

Université du Québec
INRS- ÉNERGIE, MATÉRIAUX ET TÉLÉCOMMUNICATIONS

**Comparative study based on first principles to investigate unstrained
and epitaxially strained $\text{Bi}_2\text{FeCrO}_6$ properties**

Par
Ali Almesrati

Mémoire ou thèse présentée pour l'obtention du grade de
Maître ès sciences (M.Sc.)

Jury d'évaluation

Président du jury et
examineur interne

Pr. Andreas Ruediger
(INRS-EMT)

Examineur externe

Pr. Laurent Lewis
(Université de Montréal, Département de physique)

Directeur de recherche

Pr. Alain Pignolet
(INRS-EMT)

Codirecteur de recherche

Pr. Francois Vidal
(INRS-EMT)

Abstract

Using density functional theory, we have performed a comparative study between unstrained multiferroic $\text{Bi}_2\text{FeCrO}_6$ (BFCO) and BFCO epitaxially strained on SrTiO_3 (STO) substrate. We have compared the predicted structural, magnetic, and electric properties in order to understand the effect of epitaxial strain. In this work, all calculations were performed using the LSDA+U formalism implemented in the VASP code and used a $8 \times 8 \times 8$ Monkhorst-Pack grid of k- points and a cutoff energy of 500 eV.

We have first investigated the properties of the unstrained system that has a rhombohedral symmetry and belongs to the $R\bar{3}$ space group, with lattice parameters $a_{\text{rh}}=5.47\text{\AA}$ and $\alpha_{\text{rh}}=60.09^\circ$. The lattice parameters of the BFCO unit cell obtained through spin-polarized calculations and complete relaxation. The results revealed small differences with what has been reported in literature. The differences are chiefly in the contribution of Fe and Cr to the total magnetic moment, the energy of the fully optimized structure, as well as the position of some ions. The total magnetic moment per unit cell of the ferrimagnetic high spin (FiMHS) and ferromagnetic high spin (FMHS) configurations are $1.987 \mu_B$ and $7.66 \mu_B$, respectively, while that of the ferrimagnetic low spin (FiMLS) and ferromagnetic low spin (FMLS) configurations results in values of $3.8 \mu_B$ and $1.88 \mu_B$, respectively. For completeness, the ionic charges, as well as the density of state have been calculated. Despite slight differences, our results are in overall agreement with what has been reported in the literature.

Secondly, we have investigated the effect of the epitaxial strain on the electronic and magnetic properties of the BFCO system. To this end, the lattice parameters of the rhombohedral BFCO unit cell have been fixed to the STO parameters in the plane of the BFCO/STO interface and the out-of-plane lattice parameter has been varied. We found that FiMHS remains the ground state configuration of the BFCO system under the epitaxial constraint of STO. The influence of the epitaxial deformation imposed by the STO substrate mainly manifests itself in the ionic contribution to spontaneous polarization by inducing a change of $7.64 \mu\text{C cm}^{-2}$ for the the ground state (FiMHS), and producing a total polarization estimated at $90.24 \mu\text{C cm}^{-2}$, as compared to $79.24 \mu\text{C cm}^{-2}$

in the unstrained case. The magnetic moments of the constrained and unconstrained BFCO are very similar, the main difference being observed for the FiMLS phase, with $1.905 \mu_B$ instead of $1.880 \mu_B$. Finally, we have calculated the density of states. Comparing with the case of the system without constraint, we found that the band gap remains practically unchanged for FiMHS, is reduced by 0.1 eV (-10%) for FMHS, and almost vanishes for FMLS and FiMLS.

Acknowledgement

Firstly, I would like to express my sincere gratitude to my supervisor Professor Alain Pignolet for his guidance, great support, and precious advices. I am especially thankful for the freedom he gave me to do this work.

I owe my deepest and honest thanks to my co-supervisor Professor François Vidal for his constant support, infinite patience, and his constructive suggestions which were essential in the development of this work.

I would like to take this opportunity to acknowledge the jury members for agreeing to read and evaluate this work.

There are not enough words to thank the Ph.D. candidate Mohamed Cherif for his support and encouragement.

Special thanks to Dr. Liliana Braescu who offered me insightful discussions and valuable suggestions throughout my research. I am also very grateful to Dr. Luca Corbellini who has been helpful in providing advice many times during.

Finally, I would like to thank all those who supported me during this journey: all of my family members and my friends.

Table of Contents

Acknowledgment.....	iii
List of tables.....	vii
List of figures.....	viii
List of abbreviation.....	ix
Introduction.....	1
References.....	4
Chapter 1: Density Functional Theory.....	6
1.1 Background.....	6
1.2 Schrödinger's Equation for many body systems.....	7
1.2.1 Born - Oppenheimer approximation (BOA).....	8
1.3 Thomas-Fermi model (TF).....	9
1.4 Hohenberg-Kohn Theorem (H-K theorem).....	10
1.5 Kohn-Sham Equations (KS).....	11
1.6 Local Density Approximation (LDA).....	14
1.6.1 Local Spin Density Approximation (LSDA).....	15
1.7 LDA plus Hubbard model (LDA+U).....	15
1.8 References.....	18
Chapter 2: Ferroic and Multiferroic Materials.....	19

2.0 Introduction.....	19
2.1 The Perovskite structure.....	21
2.1.1 Single perovskites.....	21
2.1.2 Double perovskites.....	22
2.2 Deviation from ideality and octahedral rotation.....	23
2.2.1 Jahn-Teller effect (JT).....	24
2.3 Ferroic materials.....	26
2.4 Ferroelectric materials.....	27
2.5 Magnetic materials.....	30
2.5.1 Diamagnetic and paramagnetic materials.....	32
2.5.2 Ferromagnetic materials.....	32
2.5.3 Ferrimagnetism and Anti-ferromagnetism.....	33
2.6 Multiferroic materials.....	34
2.7 Magnetoelectric effect.....	37
2.7.1 Direct and Inverse Magnetoelectric Effect.....	38
2.7.2 Indirect or Elastically-mediated Magnetoelectric Effect.....	39
2.8 Potential applications.....	39
2.9 References.....	40
Chapter 3: Computational Details and Results.....	43
3.1 Vienna Ab Initio Simulation Package (VASP).....	43
3.2 Introduction to Bi ₂ FeCrO ₆ (BFCO) crystal structure.....	44
3.3 Calculations for unstrained BFCO.....	46
3.3.1 Computing atomic charges.....	49
3.4 Influence of the epitaxial strain on BFCO single crystal.....	50

3.4.1 SrTiO ₃ (STO) crystal structure.....	50
3.4.2 Technical details.....	51
3.5 Variation of the energy as a function of the out-of plane-cell size.....	51
3.6 Calculations of the Electric Polarization.....	58
3.7 Density of state (DOS) calculations for strained and unstrained BFCO.....	62
3.8 References.....	66
Conclusion and Perspectives.....	67

LIST OF THE TABLES

Table 3.1 Summary of the electronic properties of the unstrained BFCO.....	48
Table 3.2 The total charge of each ion in units of the elementary charge.....	49
Table 3.3 Calculated parameters and properties of strained BFCO.....	56
Table 3.4 Total charge of each ion in unit of the elementary charge.....	57
Table 3.5 Contribution of each ion to ionic polarization.....	60
Table 3.6 Polarization results of strained and unstrained BFCO.....	61

LIST OF FIGURES

Figure 2.1: (a) Ideal perovskite structure of formula ABX_3 (b Alternate) representations of perovskite with the BO_6 octahedra at the corner of a cube and the large cation A in the middle.....	21
Figure 2.2: Ideal cubic double perovskite of formula $A_2BB'O_6$	22
Figure 2.3: Schematic representation for an ideal perovskite cubic structure.....	23
Figure 2.4: Jahn-Teller effect on octahedral copper (II) complex where the green atom represents Cu^{+2} and red atoms are usually oxygen.....	25
Figure 2.5: Hysteresis loop characteristic of a ferroelectric material, showing polarization P as a function of the applied electric field E	28
Figure 2.6: Schematic potential well (Gibbs free energy G vs. Polarization P) of a ferroelectric system with first order phase transition for $T > T_c$, $T = T_c$, and $T < T_c$. the red arrows indicate the polarization states	29
Figure 2.7: Classification of magnetic materials according to their magnetic dipole ordering..	30
Figure 2.8: Magnetic hysteresis curve of ferromagnetic material and evolution of the macroscopic magnetization M as a function of magnetic field H.....	33
Figure 2.9: Schematics representation multiferroics (green color) combining the properties of ferroelectrics (Blue color) and of magnetic materials (yellow color) , i.e. exhibiting both magnetic and ferroelectric hysteresis loops.....	35

Figure 3.1: BFCO rhombohedral structure and ordering of the transition metals Cr and Fe along the $\langle 111 \rangle$ direction. a_{BFCO_R} , Indicates the lattice constant of the rhombohedron. 10 atoms of the unit cell are identified ($\text{Bi}_1, \text{Bi}_2, \text{Cr}, \text{Fe}, \text{O}_1, \dots, \text{O}_6$).....	44
Figure 3.2: Crystal field splitting diagram for Fe^{+3} and Cr^{+3} with spin orientations in the high-spin and low-spin cases.....	45
Figure 3.3: Cubic structure of STO with lattice constant = 3.905 Å.....	51
Figure 3.4: Sketch of the rhombohedra in a highly symmetric cubic BFCO.....	53
Figure 3.5: Modifying BFCO lattice constant (\vec{a}_{BFCO_R}) to fit exactly STO lattice constant (a_{STO})	53
Figure 3.6: The relation between the energy and f. The total magnetic moment per unit cell and the quality of the fits by quartic polynomials are also shown.....	54
Figure 3.7: Energy vs. f for the four phases of BFCO (FIMLS, FMLS, FMHS, and FIMHS) and of the fit of quartic polynomials.....	55
Figure 3.8: Projected DOS of the FIMHS and FMHS phases of strained BFCO (left) and unstrained BFCO (right). Spins up and down are represented on the positive and negative vertical axis, respectively. The DOS calculations are performed with $U = 3$ eV and $J = 0.8$ eV.....	64
Figure 3.9: Projected DOS of the FIMLS and FMLS phases of strained BFCO (left) and unstrained BFCO (right). Spins up and down are represented on the positive and negative vertical axis, respectively. The DOS calculations are performed with $U = 3$ eV and $J = 0.8$ eV.....	65
Figure 4.1: Supercell represents BFCO thin film containing three layers of BFCO and two layers of STO as a substrate.....	68

LIST OF ABBREVIATIONS

BFCO	$\text{Bi}_2\text{FeCrO}_6$
DFT	Density functional theory
STO	SrTiO_3
LSDA+U	Local spin density approximation plus Hubbard model
VASP	Vienna Ab Initio Simulation Package
FiMHS	Ferrimagnetic high spin
FMHS	Ferromagnetic high spin
FiMLS	Ferrimagnetic low spin
FMLS	Ferromagnetic low spin
DOS	Density of states
BFMO	$\text{Bi}_2\text{FeMnO}_6$
BNMO	$\text{Bi}_2\text{NiMnO}_6$
BFO	BiFeO_3
BCO	BiCrO_3
TF	Thomas-Fermi
HF	Hartree-Fock
BOA	Born-Oppenheimer approximation
LDA	Local density approximation
T_N	Néel temperature

PLD	Pulsed laser deposition
JT	Jahn-Teller (effect)
PAW	Projector augmented wave (method)
BZK	Brillouin zone k-points
RWIG	Wigner –Seitz Radius
CFT	Crystal Field Theory
LAO	LaAlO ₃
LSAT	(LaAlO ₃) _{0.3} (Sr ₂ AlTaO ₆) _{0.7}

Introduction

Nowadays, the ongoing development of theories leading to the design of numerical algorithms and of electronic structure software packages has enabled the study of quite complicated physical systems with high reliability and in a reasonable time. Ab initio density functional theory (DFT), which is built on the first principles of quantum mechanics, has proven to be an astonishing tool, very successful in material science as well as in other fields. The DFT formalism relies on the electron density, instead on the wave function, in order to determine the ground state properties of a system of electrons without the need of empirical adjustable parameters.

DFT has been widely used to investigate the properties of interest in many materials. As such, it has also been among the techniques used to predict the properties of a family of materials called multiferroics. The formal definition of a multiferroic material is the simultaneous presence of more than one ferroic order in the same phase. In most cases, multiferroic materials show a ferroelectric order (often accompanied by a ferroelastic order) and a ferromagnetic or antiferromagnetic order [1]. Such a multiplicity of physiochemical properties in a single material, with promising potential applications (such as controlling the magnetic properties of the multiferroic material electrically), has attracted a significant attention. Therefore, theoretical and experimental studies are currently being dedicated to gain fundamental understanding of the magnetic and electric properties of single-phase multiferroic crystals. The valuable properties of multiferroics are mainly related to the presence of the magnetoelectric effect (interplay between electrical polarization and magnetization), which gives these materials their great significance in terms of the variety of applications they could potentially enable, particularly in electronic devices. Several bismuth-based double perovskites of the $\text{Bi}_2\text{BB}'\text{O}_6$ family, such as $\text{Bi}_2\text{FeCrO}_6$ (BFCO), $\text{Bi}_2\text{FeMnO}_6$ (BFMO), and $\text{Bi}_2\text{NiMnO}_6$ (BNMO) are promising candidates exhibiting multiferroism [2] [3] [4].

BFCO was designed by combining its parents, the Bi-based BiFeO_3 (BFO) and BiCrO_3 (BCO) in a unit cell. BFCO has attracted intensive attention in particular after the experimental observation of multiferroicity at room temperature exceeding the properties

predicted by DFT calculations [5]. The first DFT calculations to investigate BFCO properties were done by Baettig et al., and they reported that the lowest energy structure belongs to the R3 symmetry group with a rhombohedral distorted unit cell, with $a_{rh} = 5.47 \text{ \AA}$ and $\alpha_{rh} = 60.09^\circ$. The B-site of the rhombohedral structure is occupied by alternate Fe^{3+} and Cr^{3+} ions with a perfect ordering along the (111) direction. Ferromagnetism and insulating properties stem from superexchange interaction of the spatial spin arrangement of Fe-d⁵ and Cr-d³ cations, while the ferroelectricity is attributed to the Bi^{3+} with the stereochemically active 6s² lone pair of electrons. An estimation of the magnetic Curie temperature of the BFCO system was provided by calculating the exchange coupling constant of nearest neighbors through the mean-field approximation. Baettig et al. work clearly highlighted promising multiferroic properties with electric polarization of $80 \mu\text{C} \cdot \text{cm}^{-2}$ and magnetic moment of $2 \mu_B$ per formula unit (f.u.) for the ferrimagnetic ground state configuration of BFCO [6][7]. Since then, the experimental efforts relied on thin film deposition techniques, whereby strain engineering is used to enhance the multifunctional properties of BFCO epitaxial thin films. The growth of BFCO thin film was successfully obtained on SrTiO_3 (STO) substrate with a measured magnetic moment of $1.91 \mu_B/\text{f. u.}$ and a remanent polarization of $60 \mu\text{C} \cdot \text{cm}^{-2}$ [5]. These experimental findings are consistent with the DFT calculation of Ref. [6], although those calculations were done at 0 K while the ferroelectric and magnetic measurements were performed at room temperature. Calculations of Ref. [9], performed using advanced computational techniques, predicted a Curie temperature of $\sim 450 \text{ K}$. It has been recognized that the properties of materials with a perovskite structure, in particular those with a double-perovskite structure, are strongly sensitive to the influence of epitaxial strain [10]. Epitaxial strain is commonly used experimentally to control the thin film properties, and it can be simulated theoretically. When a thin film (single crystal) grows on the top of a crystalline substrate, it keeps the symmetry of the crystallographic plane forming the substrate surface and also tries to keep the lattice constants of this plane, and the overlayer is said to have grown epitaxially. The crystallographic structure of the monocrystalline overlayer thus depends on the arrangement of the atoms in the substrate as well as on its crystallographic orientation. For the case of the growth of BFCO film on STO, the structure of the film is deformed due to slightly different lattice parameters

(lattice mismatch) of the two materials. Hence, in heteroepitaxy (growth of a film of a different material than the substrate), the effects of strain are unavoidable and can influence significantly the physical properties of the investigated epitaxial thin films.

The progress in materials modeling opens the possibility to simulate the experimentally observed strain effects. Epitaxial strain can be implemented in DFT calculations by fixing the in-plane lattice parameters (a and b) which are related to the substrate, whereas relaxation of the remaining structural parameters is permitted in accord with the global energy minimum under epitaxial constraint [7]. In this regard, the influence of epitaxial strain on several Bi-based perovskite structures have been investigated. Unstrained bismuth ferrite BFO exhibits a polarization of $96 \mu\text{C cm}^{-2}$ with a very weak net ferromagnetic moment, whereas epitaxial strain calculations predicted a high intrinsic polarization up to $150 \mu\text{C cm}^{-2}$ when the tetragonal BFO structure is strongly elongated out of the plane [10]. This predicted giant ferroelectricity was indeed experimentally observed [11]. Double perovskite BFMO is another single-phase multiferroic candidate that has been investigated theoretically and experimentally demonstrated. Recently, experimental measurements at room temperature reported that BFMO-strained thin films have a magnetization value of $1.16 \mu_{\text{B}}/\text{f. u.}$ [12]. The stable state of the fully relaxed BFMO thick film predicted from non-magnetic DFT calculations has a monoclinic symmetry. In addition, a self-consistent calculation carried out on strained tetragonal BFMO predicted that the total magnetic moment depends on epitaxial strain: for a particular c/a ratio of 1.27, the total magnetic moment was found to be $1.11 \mu_{\text{B}}/\text{f. u.}$ while for $c/a = 1.45$ (experimental ratio of BFMO/STO films), the magnetic moment found was $1.05 \mu_{\text{B}}/\text{f. u.}$ [13][14]. Regarding recent work on BFCO, magnetic and electronic properties were computed by Goffinet et al. within the DFT framework [15]. Four possible magnetic configurations were examined for 4 cases of spin ordering, namely FiMLS, FiMHS, FMLS and FMHS, i.e. an antiparallel spin arrangement (ferrimagnetic – FI) and a parallel spin arrangement (ferromagnetic – FM), for both high spin (HS) and low spin (LS) configurations of iron. The results showed that the FiMHS configuration represents the ground state of the BFCO system with a magnetic moment of $2 \mu_{\text{B}}$ per unit cell (in agreement with previous works), while the FMHS is predicted to have a slightly higher energy than the ground state. They found that reducing the volume of the unit cell leads

to a crossover between FiMLS and FiMHS as the lowest energy state (however, both states have the same magnetic moment of $2 \mu_B$). More recently, DFT was employed in order to investigate the influence of epitaxial strain on BFCO by using a tetragonal supercell involving 20 atoms. Interestingly, a magnetic moment of $2 \mu_B/f. u.$ was reported [16].

The main objectives of this work are to investigate the properties of epitaxially strained rhombohedral BFCO on a STO substrate within the framework of DFT calculations in order to compare the obtained results with those obtained for unstrained BFCO. As we mentioned previously, it is expected that BFCO properties are affected by the epitaxial strain and, toward this end, we imposed the value of the STO lattice parameter to the pseudo-cubic lattice parameter of rhombohedral BFCO in order to simulate the strained BFCO epitaxial thin film. In the simulation, we fixed the in-plane parameters and varied manually the out-of-plane parameter of the unit cell. We performed full relaxation within these constraints. In contrast, all the structural parameters of unstrained BFCO are fully relaxed. Electric and magnetic properties were investigated in both cases. At the end, we come up with a comparison between strained and unstrained BFCO.

References

1. H. Schmid, *Ferroelectrics*, 162,317 (1994)
2. S. Kamba, D. Nuzhnyy, R. Nechache, K. Zaveta, D. Niznansky, E. antava, C.Harnagea, and A. Pignolet, *Phys. Rev. B* 77, 104111 (2008)
3. Lei Bi, A. R. Taussig, Hyun-Suk Kim, Lei Wang, G. F. Dionne, D. Bono, K. Persson, G. Ceder, and C. A. Ross, *Phys. Rev. B* 78, 104106 (2008)
4. M. N. Iliev, P. Padhan, and A. Gupta, *Phys. Rev. B* 77, 172303 (2008)
5. R. Nechache, C. Harnagea, L. P. Carignan, et al, *J. Appl. Phys.* 105, 061621 (2009)
6. P. Baettig, C. Ederer, N.A. Spaldin, *Phys. Rev. B* 72, 214105 (2005)
7. P. Baettig, N.A. Spaldin, *Appl. Phys. Lett.* , 86, 012505 (2005)
8. S. Picozzi and, C. Ederer, *J. Phys.: Condens. Matter*, 21 303201 (2009)
9. Song Zhe-Wen, Liu Bang-Gui, *Chin. Phys. B* Vol. 22, No. 4, 047506 (2013)
10. A. J. Hatt, N. A. Spaldin, C. Ederer, *Phys. Rev. B* 81, 054109 (2010)
11. E.-M. Choi, S. Patnaik, E. Weal, S.-L. Sahonta, H. Wang, Z. Bi, J. Xiong, M. G. Blamire, Q. X. Jia, and J. L. MacManusDriscoll, *Appl. Phys. Lett.* 98, 012509 (2011)

12. L. Bi, A. R. Taussig, H.-S. Kim, L. Wang, G. F. Dionne, D. Bono, K. Persson, G. Ceder, and C. A. Ross, *Phys. Rev. B* 78,104106 (2008)
13. T.Ahmed, A.Chen, D. A. Yarotski, S. A. Trugman, Q. Jia, and Jian-Xin Zhu, *APL Materials* 5, 035601 (2017)
14. M. Goffinet, J. Iniguez, and P. Ghosez, *Phys. Rev. B* 86, 024415 (2012)
15. P. C. Rout, A. Putatunda, and V. Srinivasan, *Phys. Rev. B* 93, 104415, (2016)
16. A. Khare, A. Singh, S. S. Prabhu, and D. S. Rana, *Appl. Phys.ett.* 102, 192911 (2013)

Chapter 1. DENSITY FUNCTIONAL THEORY

1.1 Background

The first vision of density functional theory (DFT) started from Thomas and Fermi (TF) in 1920. The TF model was designed to calculate the electron distribution inside the atom. In 1928, Dirac improved the TF work by adding exchange energy density. However, the theory of Thomas-Fermi-Dirac was inaccurate for most applications due to the weak representation of the kinetic energy as a function of the electron density and to the absence of electron correlation in the model. Ab initio (first principles) methods with various approximations and assumptions have been developed to study the properties of many-body-systems [1]. The Hartree-Fock (HF) method is the simplest ab initio method for treating interacting systems. This method assumes that the electron can affect the average potential created by the other electrons. In fact, considerable complications occur due to considering single electron orbitals and solving many wave functions. The difficulty of using HF calculations increases as the number of electrons goes up [2].

In 1964, Hohenberg and Kohn introduced the bases of DFT. Their main idea was to determine the electronic ground state energy of the system from the electron density. According to their work, the electron density of the ground state not only uniquely determines the total energy of the ground state but also all the other system's properties. Since the electron density is a single three-dimensional distribution in space, there is no need to calculate the wave function of each electron in the system as in the HF method. In order to specify the energy of the ground state corresponding to the electron density, it is necessary to formulate a functional relating these two quantities.

The year after, Kohn and Sham introduced the exchange correlation functional, which relates the electron density to the ground state energy. The Kohn-Sham method is a mathematical model based on a non-interacting electrons system. In their approximated approach, the exchange correlation functional takes into account the quantum interaction between electrons [3].

The main objective of this chapter is to introduce the basics of DFT, starting from the resolution of the non-relativistic Schrödinger's equation.

1.2 Schrödinger's Equation for Many Body Systems

Resolving the Schrödinger's equation for many body systems has been attempted since quantum mechanics emerged. Analytically, obtaining the exact solution for a system having more than two electrons is however impossible [4]. In quantum mechanics, all the observable quantities can be obtained from the system's wave function Ψ . In a stationary system, this wave function is calculated from the non-relativistic time-independent Schrödinger's equation, which for a distribution of electrons and nuclei can be written generally as

$$\{H - E\}\Psi(r, R) = 0 \quad (1.1)$$

where E is the total energy of the system and the Hamiltonian given by

$$H = T + V_{e-e} + V_{e-n} + V_{n-n} \quad (1.2)$$

Here r and R represent collectively the positions of the electrons and of the nuclei, respectively. In Eq. (1.2), T is the kinetic energy of the electrons and nuclei, V_{e-e} is the potential energy due to electron-electron interaction, V_{e-n} is the potential energy of the electron-nuclei interaction, and V_{n-n} is the nuclei-nuclei interaction. The wave function $\Psi(r, R)$ depends on the positions and spin coordinates of all N nuclei and n electrons in the system.

In the following we use the atomic units $\hbar = e = 4\pi\epsilon_0 = m_e = 1$. For a normalized distribution of electrons with coordinates r_i and nuclei with charges Z_a and coordinates R_a , the terms of Eq. (1.2) can be written (ignoring the spin-spin and spin-orbit interactions here for simplicity),

$$\begin{aligned} T &= -\frac{1}{2}\{\sum_{\mu} \nabla_{\mu}^2 + \sum_a \frac{1}{M_a} \nabla_a^2\}; \\ V_{e-e} &= +\frac{1}{2}\sum_{\mu, \nu(\mu \neq \nu)} \frac{1}{|\mathbf{r}_{\mu} - \mathbf{r}_{\nu}|} ; \\ V_{e-n} &= -\sum_{\mu, a} \frac{Z_a}{|\mathbf{r}_{\mu} - \mathbf{R}_a|} ; \\ V_{n-n} &= +\frac{1}{2}\sum_{a, b(a \neq b)} \frac{Z_a Z_b}{|\mathbf{R}_a - \mathbf{R}_b|} ; \end{aligned}$$

The kinetic energy T involves a sum over all electrons ($\mu = 1 \rightarrow n$) and nuclei ($\alpha = 1 \rightarrow N$). The electron-electron and nuclei-nuclei potentials are the sum over all combinations of distinct pairs. To avoid each pair from being counted twice, the potentials V_{e-e} and V_{n-n} are multiplied by $\frac{1}{2}$.

1.2.1 Born - Oppenheimer approximation (BOA)

The BOA is a simplification that has been used almost in all methods to solve Schrödinger's equation for atomic systems. It is well known that the charge magnitude is the same for electrons and protons while the mass ratio of electron to the proton is $1/1836$. Since the mass of the nuclei is much greater than the electron's mass, electrons can move much faster than the nuclei. Hence, the electron distribution will change rapidly with the variation of the nuclei field [5]. Therefore, it is possible to consider the position of the nuclei \mathbf{R} as fixed relative to the electrons motion. Accordingly, BOA allows to decouple the total wavefunction into the electronic part and nuclear part. This is also called the adiabatic approximation. In this way, the total wave function for fixed nuclear arrangement, $\Psi(r, R)$, can be expressed as an expansion over the set of adiabatic electron wavefunctions $\varphi_k(r, R)$:

$$\Psi(\mathbf{r}, \mathbf{R}) = \sum_k \chi_k(\mathbf{R}) \varphi_k(\mathbf{r}, \mathbf{R}) \quad (1.3)$$

where $\chi_k(\mathbf{R})$ is the expansion coefficients depending only on the parameter \mathbf{R} . The $\varphi_k(\mathbf{r}, \mathbf{R})$ satisfy the following wave equation for electrons:

$$\left\{ -\frac{1}{2} \sum_{\mu} \nabla_{\mu}^2 + V_{e-e} + V_{e-n} + V_{n-n} \right\} \varphi_k(\mathbf{r}, \mathbf{R}) = E_k(\mathbf{R}) \varphi_k(\mathbf{r}, \mathbf{R}) \quad (1.4)$$

where we assumed that the kinetic energy of the nuclei is zero.

In order to obtain the nuclear wave function, we write the full Schrödinger Eq. (1.1) as

$$\left\{ -\frac{1}{2} \sum_n \frac{1}{M_n} \nabla_n^2 + H_e \right\} \Psi(\mathbf{r}, \mathbf{R}) = E \Psi(\mathbf{r}, \mathbf{R}) \quad (1.5)$$

Where H_e is the electron Hamiltonian expressed by the terms in brackets in Eq. (1.4) (by convention, the constant V_{n-n} is also included in H_e). Eq. (1.5) can also be written as

$$\sum_k \varphi_k(\mathbf{r}, \mathbf{R}) \left\{ -\frac{1}{2} \sum_n \frac{1}{M_n} \nabla_n^2 + E_k(\mathbf{R}) - E \right\} \chi_k(\mathbf{R}) = \sum_k \sum_n \frac{1}{2M_n} \{ \chi_k(\mathbf{R}) \nabla_n^2 \varphi_k(\mathbf{r}, \mathbf{R}) + 2 \nabla_n \chi_k(\mathbf{R}) \cdot \nabla_n \varphi_k(\mathbf{r}, \mathbf{R}) \} \quad (1.6)$$

which is decoupled from the electronic movement. Considering Eq. (1.6) together with Eq. (1.4), one sees that the description of the nuclear and electronic movements can be made separately [6].

1.3 Thomas –Fermi (TF) Model

Thomas and Fermi considered an ideal system relying on the kinetic energy of non-interacting electrons. The TF model approximates the electron distribution in the atom as a homogeneous gas [7]. If electrons behave as independent fermionic particles at zero Kelvin, the energy levels of the electrons in cubic potential well are given by

$$E(n_x, n_y, n_z) = \frac{\pi^2}{2l^2} (n_x^2 + n_y^2 + n_z^2) \quad (1.7)$$

where n_x, n_y, n_z are integer numbers and l is the length of the cubic edge.

The Fermi energy corresponds to the highest energy level for N electrons in a volume $V = l^3$, respecting the Pauli principle, and is given by:

$$\epsilon_F(\rho) = \frac{1}{2} (3\pi^2 \rho)^{2/3} \quad (1.8)$$

where $\rho = N/V$ is the electron density. For this electron density, the kinetic energy density is given by

$$\int_0^\rho \epsilon_F(\rho') d\rho' = \frac{3}{5} \epsilon_F(\rho) \rho = C_F \rho^{5/3} \quad (1.9)$$

where $C_F = \frac{3}{10} \left(\frac{3}{8\pi} \right)^{2/3}$.

The total energy of a system, submitted to an external potential $V_{ext}(\mathbf{r})$, thus depends only on the electron density ρ and is given by the sum of the kinetic and potential energies

$$E_{TF}[\rho] = C_F \int [\rho(\mathbf{r})]^{5/3} d\mathbf{r} + \int \rho(\mathbf{r}) V_{ext}(\mathbf{r}) d\mathbf{r} + \iint \frac{\rho(\mathbf{r})\rho(\mathbf{r}')}{|\mathbf{r}-\mathbf{r}'|} d\mathbf{r} d\mathbf{r}' \quad (1.10)$$

Eq. (1.10) shows that the electron density can be used instead of the wavefunction to describe the total energy of the electronic system.

The TF model is accurate only if the system consists of one atom. Although the TF model fails to describe large systems, it is considered as the starting point to DFT (Hohenberg and Kohn theorem) [8].

1.4 Hohenberg-Kohn Theorem (H-K theorem)

The first H-K theorem states that for systems containing N electrons in an external potential $V(\mathbf{r})$ (Coulomb potential usually generated by the nuclei), the external potential $V(\mathbf{r})$ is completely determined by the electron density $\rho(\mathbf{r})$ associated with the ground state energy [9].

To prove that, consider the Hamiltonian of a many-body system:

$$H = -\sum_{i=1}^N \frac{1}{2} \nabla_i^2 + \sum_{i<j}^N U(\mathbf{r}_i, \mathbf{r}_j) + \sum_{i=1}^N V(\mathbf{r}_i) \equiv T + U + V \quad (1.11)$$

where T is the kinetic energy, U the energy of electron-electron interaction, and V is the external potential. The electron density is defined as

$$\rho(\mathbf{r}) = N \int |\Psi(\mathbf{r}, \mathbf{r}_2, \dots, \mathbf{r}_N)|^2 d\mathbf{r}_2 \dots d\mathbf{r}_N \quad (1.12)$$

where Ψ is the electron wave function. Consider now a Hamiltonian $H' = T + U + V'$ where $V - V' \neq \text{const}$. The wave function of the ground state for H' is Ψ' . Then we have the following inequality:

$$E' = \langle \Psi' | H' | \Psi' \rangle < \langle \Psi | H' | \Psi \rangle \quad (1.13)$$

where

$$\begin{aligned} \langle \Psi | H' | \Psi \rangle &= \langle \Psi | T + U + V + V' - V | \Psi \rangle \\ &= E + \langle \Psi | V' - V | \Psi \rangle \\ &= E + \int \rho(\mathbf{r}) [V'(\mathbf{r}) - V(\mathbf{r})] d\mathbf{r} \end{aligned}$$

Now, assume that the electron density $\rho(\mathbf{r})$ is the same for both H and H' . Then a similar inequality must hold when inverting the prime and nonprime quantities:

$$E < E' + \int \rho(\mathbf{r})[V(\mathbf{r}) - V'(\mathbf{r})]d\mathbf{r}$$

Adding up the last two inequalities, one finds $E' + E < E + E'$. This contradiction implies the impossibility of associating the same electron density $\rho(\mathbf{r})$ to both external potentials $V(\mathbf{r})$ and $V'(\mathbf{r})$. Therefore, the external potential is uniquely determined by the electron density $\rho(\mathbf{r})$, as stated in the first H-K theorem.

The second H-K theorem states that the ground state energy can be obtained from a variational principle, i.e. the density that minimises the total energy is the exact ground state density. The proof is also straightforward. We can represent the energy as the functional

$$E[\rho(\mathbf{r})] = \langle \Psi | T + U | \Psi \rangle + \langle \Psi | V | \Psi \rangle = F[\rho(\mathbf{r})] + \int \rho(\mathbf{r})V(\mathbf{r})d\mathbf{r} \quad (1.14)$$

where $F[\rho(\mathbf{r})]$ is a universal functional depending only on the electron density $\rho(\mathbf{r})$. The variational principle states that:

$$\langle \Psi' | T + U + V | \Psi' \rangle > \langle \Psi | T + U + V | \Psi \rangle$$

We thus obtain:

$$E[\rho'(\mathbf{r})] > E[\rho(\mathbf{r})]$$

which implies that the density that minimises the total energy is the exact ground state density and proves the theorem.

1.5 Kohn-Sham (KS) Equations

Since the kinetic energy of the system of interacting electrons is unknown, Kohn and Sham proposed to replace the system of interacting electrons by a system of non-interacting electrons evolving in an effective potential, imposing that the electron density in the ground state is the same for both systems [\[10\]\[11\]](#). This amounts to replace the Hohenberg-Kohn functional (1.14)

$$E_{HS}[\rho] = F[\rho] + \int \rho(\mathbf{r})V(\mathbf{r})d\mathbf{r}$$

by the following one

$$E_{KS}[\rho] = T_{KS}[\rho] + J[\rho] \quad (1.15)$$

where is $T_{KS}[\rho]$ is the non-interacting kinetic energy and

$$J[\rho] = V + U + (T - T_{KS})$$

Therefore:

$$E_{KS}[\rho(\mathbf{r})] = -\sum_i \left\langle \Psi_i \left| \frac{1}{2} \nabla_i^2 \right| \Psi_i \right\rangle + \frac{1}{2} \int \int \frac{\rho(\mathbf{r})\rho(\mathbf{r}')}{|\mathbf{r}-\mathbf{r}'|} d\mathbf{r}d\mathbf{r}' + E_{XC}[\rho(\mathbf{r})] + \int \rho(\mathbf{r})V(\mathbf{r}) d\mathbf{r}$$

where the Ψ_i form a set of functions (called orbitals) so that

$$\rho(\mathbf{r}) = \sum_i f_i |\Psi_i(\mathbf{r})|^2$$

where f_i is the number of electrons in the orbital i (normally $f_i = 2$).

In $E_{KS}[\rho]$, the first term is the kinetic energy and the second term is the Hartree term that takes into account the repulsion of the electron cloud. The term $E_{XC}[\rho]$ is the exchange-correlation term, which represents everything that is not taken into account by the other terms. The exchange term is a quantum mechanical effect producing a pseudo force between electrons that results from their undistinguishable nature. The correlation term describes the departure from the non-interacting electron assumption.

The orbital functions Ψ_i are obtained by minimizing the energy $E_{KS}[\rho]$ under the orthonormal constraints $\int \Psi_i^*(\mathbf{r}) \Psi_j(\mathbf{r})d\mathbf{r} = \langle \Psi_i | \Psi_j \rangle = \delta_{ij}$. This is done using the variational method of Lagrange multipliers

$$\delta\{E[\rho(r)] - \sum_{ij} \lambda_{ij} (\int \Psi_i^*(\mathbf{r}) \Psi_j(\mathbf{r})d\mathbf{r} - \delta_{ij})\} = 0 \quad (1.16)$$

where the operator δ denotes an arbitrary variation of Ψ_i . In this expression, the λ_{ij} are the Lagrange multipliers such that $\lambda_{ij} = \delta_{ij}\epsilon_j$ due to the orthonormality condition of the Ψ_i . One thus has to solve the following variation equation for $\rho(\mathbf{r})$:

$$\delta\{E[\rho(\mathbf{r})] - \sum_i \epsilon_i \int \Psi_i^*(\mathbf{r})\Psi_i(\mathbf{r}) d\mathbf{r}\} = 0 \quad (1.17)$$

The various terms in this equation can be developed as follows:

$$\delta \sum_i \int \Psi_i^*(\mathbf{r}) \nabla_i^2 \Psi_i(\mathbf{r}) d\mathbf{r} = 2\text{Re} \left[\sum_i \int \delta \Psi_i^*(\mathbf{r}) \nabla_i^2 \Psi_i(\mathbf{r}) \right]$$

where Re denotes the real part of the argument. Furthermore,

$$\begin{aligned} & \delta \sum_{ij} \int \Psi_i^*(\mathbf{r}) \Psi_i(\mathbf{r}) \frac{1}{|\mathbf{r}-\mathbf{r}'|} \Psi_j^*(\mathbf{r}') \Psi_j(\mathbf{r}') d\mathbf{r} d\mathbf{r}' \\ &= 4\text{Re} \left[\sum_{ij} \int \delta \Psi_i^*(\mathbf{r}) \Psi_i(\mathbf{r}) \frac{1}{|\mathbf{r}-\mathbf{r}'|} \Psi_j^*(\mathbf{r}') \Psi_j(\mathbf{r}') d\mathbf{r} d\mathbf{r}' \right] \end{aligned}$$

In addition,

$$\delta \sum_i \int \Psi_i^*(\mathbf{r}) \Psi_i(\mathbf{r}) V(\mathbf{r}) d\mathbf{r} = 2\text{Re} \left[\sum_i \int \delta \Psi_i^*(\mathbf{r}) \Psi_i(\mathbf{r}) V(\mathbf{r}) d\mathbf{r} \right]$$

and,

$$\delta E_{XC}[\rho(\mathbf{r})] = \frac{\delta E_{XC}}{\delta \rho(\mathbf{r})} \delta \sum_i \int \Psi_i^*(\mathbf{r}) \Psi_i(\mathbf{r}) = \frac{\delta E_{XC}}{\delta \rho(\mathbf{r})} 2\text{Re} \left[\sum_i \int \delta \Psi_i^*(\mathbf{r}) \Psi_i(\mathbf{r}) \right]$$

Eq. (1.17) thus becomes

$$\begin{aligned} & \sum_i \left\{ \int \delta \Psi_i^*(\mathbf{r}) \left[-\frac{1}{2} \nabla_i^2 + \sum_j \int \Psi_j^*(\mathbf{r}') \frac{1}{|\mathbf{r}-\mathbf{r}'|} \Psi_j(\mathbf{r}') d\mathbf{r}' + \frac{\delta E_{XC}}{\delta \rho(\mathbf{r})} \right. \right. \\ & \left. \left. + V(\mathbf{r}) - \epsilon_i \right] \Psi_i(\mathbf{r}) d\mathbf{r} \right\} = 0 \end{aligned}$$

This is satisfied for an arbitrary variation $\delta \Psi_i^*$ only if

$$\left[-\frac{1}{2} \nabla_i^2 + V_{KS}(\mathbf{r}) \right] \Psi_i(\mathbf{r}) = \epsilon_i \Psi_i(\mathbf{r}) \quad (1.18)$$

where

$$V_{KS}(\mathbf{r}) = \int \frac{\rho(\mathbf{r}')}{|\mathbf{r}-\mathbf{r}'|} d\mathbf{r}' + \frac{\delta E_{XC}}{\delta \rho(\mathbf{r})} + V(\mathbf{r}) \quad (1.19)$$

is the K-S potential. The total energy is given by

$$E = \sum_i \epsilon_i + E_{XC} - \int \frac{\rho(\mathbf{r})\rho(\mathbf{r}')}{|\mathbf{r}-\mathbf{r}'|} d\mathbf{r}d\mathbf{r}' - \int \frac{\delta E_{XC}}{\delta \rho} \rho(\mathbf{r}) d\mathbf{r}$$

The K-S Eq. (1.18), is solved in a self-consistent way for the wavefunctions Ψ_i and their eigenvalues ϵ_i . This consists in starting from an initial guess for $\rho(\mathbf{r})$, then to calculate $V_{KS}(\mathbf{r})$ and then to solve the Kohn-Sham equation for the $\Psi_i(\mathbf{r})$. Then a new $\rho(\mathbf{r})$ is calculated and all the operations are repeated until convergence is obtained.

Although the approach of Kohn and Sham is exact, so far the exchange correlation functional $E_{KS}[\rho]$ is unknown, and therefore it is necessary to apply approximations to this functional. The Local Density Approximation (LDA) discussed in the next section is the simplest approximation.

1.6 Local Density Approximation (LDA)

In the K-S equation the exchange-correlation term $\frac{\delta E_{XC}}{\delta \rho(\mathbf{r})}$ remains to be determined. Hence, resolving this difficulty is crucial. Toward this end, a simple approximation was presented by K-S in 1965. This approach is known as LDA for energy exchange and correlation. These authors showed that if ρ varies extremely slowly with position then E_{XC} energy can be expressed by [12][13]

$$E_{XC}^{LDA}[\rho] = \int \rho(\mathbf{r}) \epsilon_{XC}(\rho) d\mathbf{r} \quad (1.20)$$

The potential entering the Kohn-Sham equation associated with this functional is

$$V_{XC}^{LDA} = \frac{\delta E_{XC}^{LDA}}{\delta \rho} = \epsilon_{XC}(\rho(\mathbf{r})) + \rho(\mathbf{r}) \frac{\partial \epsilon_{XC}(\rho)}{\partial \rho}$$

In LDA, the functional $\epsilon_{XC}(\rho)$ is expressed as the exchange energy plus the correlation energy of a homogeneous electron gas with density ρ

$$\epsilon_{XC}(\rho) = \epsilon_X(\rho) + \epsilon_c(\rho) \quad (1.21)$$

The exchange term for a homogeneous electron gas is known analytically to be

$$\epsilon_X(\rho) = -\frac{3}{4} \left(\frac{3}{\pi}\right)^{1/3} \rho^{1/3}. \quad (1.22)$$

The correlation energy per particle of a homogeneous electron gas $\epsilon_c(\rho)$ is not known analytically except in the low- and high-density limits. That is why it had to be simulated

using Quantum Monte Carlo (QMC) methods and then fitted into an analytical form. For example, the simple Chachiyo 2016 fit function [14] reads

$$\varepsilon_c(\rho) = a \ln \left(1 + \frac{b}{r_s} + \frac{b}{r_s^2} \right)$$

Here a and b are fitting parameters which can also be determined from the known limiting cases.

1.6.1 Local Spin Density Approximation (LSDA)

For spin-polarized systems, the exchange-correlation functional E_{XC} now depends on the spin up and spin-down density, ρ^\uparrow and ρ^\downarrow , respectively. The potentials entering the K-S equation for exchange and correlation are now

$$V_{XC}^\uparrow = \frac{\delta E_{XC}[\rho^\uparrow, \rho^\downarrow]}{\delta \rho^\uparrow}$$

$$V_{XC}^\downarrow = \frac{\delta E_{XC}[\rho^\uparrow, \rho^\downarrow]}{\delta \rho^\downarrow}$$

for spin up and spin down, respectively. The exchange term is simply expressed in terms of the spin unpolarised functional as

$$E_x[\rho^\uparrow, \rho^\downarrow] = \frac{1}{2} (E_x[2\rho^\uparrow] + E_x[2\rho^\downarrow]) \quad (1.24)$$

For the correlation energy density, it is necessary to introduce a different scheme to approximate the functional. The idea is to start from the energy of the fully polarized homogeneous system and then introduce the relative spin polarization

$$\zeta = \frac{\rho^\uparrow - \rho^\downarrow}{\rho^\uparrow + \rho^\downarrow}$$

If $\zeta = 0$ we have the spin-unpolarized case, which means that the electron gas is paramagnetic. If $\zeta = \pm 1$ the electron gas is fully spin polarized, corresponding to the ferromagnetic case.

Although LDA is widely used, it does not work at all to describe strongly correlated system since it fails at predicting a band gap. For such systems, one has to use the LDA+U approach.

1.7 LDA plus Hubbard model (LDA+U)

Mott insulators are an important class of material whose insulating properties result from strong electron-electron interactions (strongly correlated system) of orbitals d or f . BFCO falls into this category. LDA cannot describe Mott insulators since it is based on a simple one-electron theory. A way to correct the failure of LDA is to take explicitly into account the interaction between d (or f) electrons through a Hubbard-like model, which describes the transition between conducting and insulating systems. In this model, electrons are separated into two systems (for simplicity, we will restrict the discussion to the spin-independent case) [15]

(i) delocalized s and p electrons, which can still be described by using an orbital-independent one-electron potential (LDA);

(ii) localized d or f electrons taking into account Coulomb d - d interaction.

In the Hubbard-like model, the corrected LDA functional reads

$$E^{LDA+U} = E^{LDA} + U \sum_{i \neq j} n_i n_j / 2 - \frac{UN(N-1)}{2} \quad (1.25)$$

where U is the Coulomb repulsion parameter, n_i are the d -orbital occupancies (*i.e.* the number of electrons occupying a given d orbital i) and $N = \sum n_i$.

The second term of Eq. (1.25) takes into account the interactions between electrons in d orbital while the last term is called the double counting term which needs to be subtracted from the second term. The exchange parameter, usually denoted J , which describes the exchange interaction of electrons on neighboring sites as a consequence of the fermionic nature of the electrons, can be incorporated in the corrected LDA functional by replacing U by $U_{\text{eff}} = U - J$. In some more accurate formulations, U and J appear in separate terms [16].

Energies of the orbitals are the derivatives of Eq. (1.25) with respect to n_i

$$\epsilon_i^{LDA+U} = \frac{\partial E^{LDA+U}}{\partial n_i} = \epsilon_i^{LDA} + U \left(\frac{1}{2} - n_i \right) \quad (1.26)$$

From this expression, two main cases can be distinguished.

Case 1: If $n_i = 0$, orbitals are unoccupied and the orbital energy of LDA changes by $+U/2$.

Case 2: If $n_i \geq 1$, then orbitals are occupied and the orbital energy shifts by at least $-U/2$

The potential entering in the K-S equation,

$$V_i(\mathbf{r}) = \frac{\delta E}{\delta n_i(\mathbf{r})} = V_{LDA}(\mathbf{r}) + U \left(\frac{1}{2} - n_i \right) \quad (1.27)$$

which is orbital dependent, thus provides a description for lower and upper Hubbard bands with the energy separation between them equal to the Coulomb parameter U .

1.8 References

1. R. M., Dreizler Gross E.K.U. Introduction. In: Density Functional Theory. Springer, Berlin, Heidelberg (1990)
2. D. R. Hartree. Proc. Camb. Philos. Soc., 24, 89 (1927)
3. V. Sahni, The Hohenberg-Kohn Theorems and Kohn-Sham Density Functional Theory. In: Quantal Density Functional Theory. Springer, Berlin, Heidelberg, (2004)
4. K. Capelle , A bird's-eye view of density-functional theory, Brazilian Journal of Physics (2006)
5. M. Born; J. Robert Oppenheimer , Zur Quantentheorie der Molekeln “On the Quantum Theory of Molecules” (1927)
6. http://www.diss.fuberlin.de/diss/servlets/MCRFileNodeServlet/FUDISS_derivate_000000012723/Accardi_2012.pdf
7. <http://www.math.mcgill.ca/gantumur/math580f12/ThomasFermi.pdf>
8. E. H. Lieb, and B. Simon: The Thomas-Fermi theory of atoms, molecules and solids, Adv. in Math 23 (1977)
9. P. Hohenberg and W. Kohn. Phys. Rev., 136:864B (1964)
10. W.Kohn and L.J.Sham. Phys. Rev., 140A:1133 (1965)
11. W. Koch and M. C. Holthausen. A Chemist’s Guide to Density Functional Theory. Wiley, New York, (2000)
12. C. Fiolhais ,F. Nogueira ,M. Marques, A Primer in Density Functional Theory, Springer (2003)

13. Parr, G .Robert; Yang, Weitao, Density-Functional Theory of Atoms and Molecules, Oxford: Oxford University Press (1994)
14. T. Chachiyo, J. Chem. Phys. 145 (2): 021101 (2016)
15. U. von Barth , L. Hedin, J. Phys. C: Solid State Phys (1972)
16. V. I. Anisimov, I. V. Solovyev, M. A. Korotin, M. T. Czyzyk, and G. A. Sawatzky, Phys. Rev. B 48, 16929 (1993)

Chapter 2. FERROIC and MULTIFERROIC MATERIALS

2.0 Introduction

Historically, a magnetoelectric effects have been observed as early as 1888 by Wilhelm Röntgen, who observed that dielectrics moving through an electric field became magnetized [1]. Then in 1894, and based on symmetry analysis only, Pierre Curie without using the term ‘multiferroic’ opened this field of investigation in predicting that an electric polarization of a molecule would be obtained by applying an external magnetic field. Conversely, a magnetic moment would be induced by an external electric field [2].

In 1926, the terminology “magnetoelectric” (ME) was used for the first time by Debye to describe this phenomenon, and it was then mathematically described in their famous theoretical physics book series by L. D. Landau and E. Lifshitz in 1957, where they showed that, for certain symmetries and magnetic structures, a magnetoelectric response would be observed [3]. A few years later, in 1959, according to symmetry considerations, the form of the linear magnetoelectric effect in anti-ferromagnetic Cr_2O_3 was predicted by Dzyaloshinskii [4]. A year later, Astrov confirmed this prediction by observing experimentally that magnetization can be controlled by applying an electric field [5]. Despite the fact that interest in magnetoelectrics persisted over the next 45 years, over 80 magnetoelectric materials being discovered, a renewed surge of interest started again in 2005, together with a renewed interest in multiferroics [6].

Despite the mystery surrounding the presence of two ferroic (or more than two) orders in a single phase, a growing interest in these enigmatic materials resurfaced since the terminology of “multiferroic magnetoelectric” materials was introduced by Schmid in 1994 [7]. Thereafter, in 2000, Nicola A. Hill explained why ferromagnetic ferroelectric coexistence is so rare [8]. In 2003, a qualitative progress in this field was achieved when the group of Ramesh was able to obtain a high ferroelectric polarization through growing a single perovskite BiFeO_3 epitaxially. The discovery of a magnetoelectric coupling in Terbium manganites (TbMnO_3 , TbMn_2O_5) followed shortly after [9][10]. In BFCO the Bi^{+3} are likely responsible for the ferroelectric effect while the insulating character is ascribed

to the partially occupied subshell d^5 and d^3 of Fe^{+3} and Cr^{+3} , respectively [11]. Using first-principles calculations within the LSDA+U formalism, the lowest energy of BFCO was found to belong to the $R\bar{3}$ space group. DFT calculations show that the most stable state of BFCO corresponds to the ferrimagnetic high spin (FIHS) configuration and that changing the volume of the rhombohedral unit cell, while preserving the cell shape, BFCO exhibits a crossover between the ferrimagnetic high-spin and the ferrimagnetic low spin phases, which becomes more energetically favorable at low volumes [13]. An estimation of the magnetic arrangement vs. temperatures of BFCO was obtained by calculating the exchange coupling constant of the nearest neighbors through the mean-field approximation and first-principles calculations [11]. It was found not to exceed Néel temperature T_N equals to 100 K.

Experimentally, epitaxial thin films of BFCO grown on $SrTiO_3$ (STO), synthesized using pulsed laser deposition (PLD), clearly presented multiferroic properties at room temperature [12]. This finding confirmed in part the theoretical predictions of Ref. [11]. DFT calculations show the most stable state of BFCO corresponds to the ferrimagnetic high spin configuration and that changing the volume of the unit cell, BFCO exhibits a crossover between two ferrimagnetic phases [13].

This chapter contains a short introduction to perovskite structures and a general presentation of ferroic materials. The last part of the chapter is devoted to multiferroic materials and their potential applications.

2.1 The Perovskite Structure

2.1.1 Single Perovskites

The perovskites have a chemical formula ABX_3 , where **A** and **B** are both metallic cations and **X** is an anion (usually an oxygen atom). The structure of the perovskites can be described by its unit cell. There are two different ways to describe the ideal high-symmetry cubic perovskite unit cell: (i) The large **A** atoms are located on the corner of a cube, a smaller **B** atom is located in the center of the cube and **X** atoms (very often oxygen atoms) are located in the center of each face of the cube, so that they form an octahedron with the **B** atom in its center, as shown in Figure 2.1a. (ii) Alternately, the unit cell of the perovskite structure can be described with the small **B** atoms at the corner of a cube, each **B** atom being surrounded by an octahedron of **X** atoms, and the large **A** atom in the center of the cube, as shown in Figure 2.1b [14].

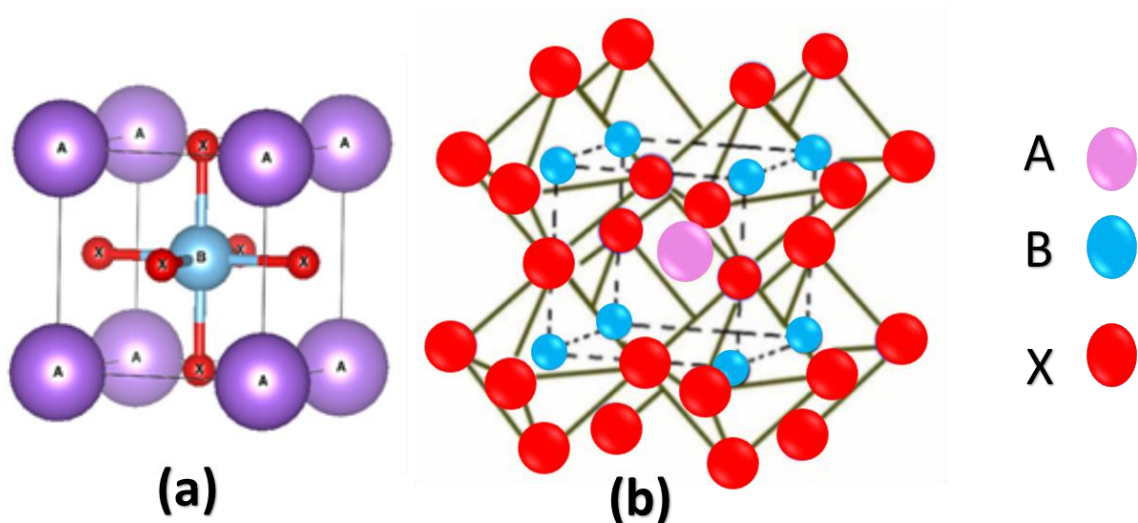


Figure 2.1. (a) Ideal perovskite structure of formula ABX_3 (b) Alternate representations of perovskite with the BO_6 octahedra at the corner of a cube and the large cation **A** in the middle.

In the ideal case of a non-polar phase, the single-perovskite structure has a cubic symmetry. Most of the polar phases having a single perovskite structure are distorted in

order to have a polar axis along which the spontaneous polarization can develop, and thus have a tetragonal, an orthorhombic or a rhombohedral symmetry.

2.1.2 Double Perovskites

In this work we are interested in more complex perovskite structures called double-perovskites. This type of perovskite can be seen as the periodic arrangement of two single perovskite ABO_3 and $AB'O_3$ unit cells with the same cation A and distinct cations B and B' positioned alternately in the 3 directions of space, which is shown in Figure 2.2. It can be seen as a rock-salt structure (like NaCl) arrangement of BO_6 and $B'O_6$ oxygen octahedra with A cations in the remaining spaces. For the ideal double perovskites, the existence of the two cations B and B' in the rock-salt structure causes a reduction of the symmetry of the single perovskite from $Pm-3m$ to $Fm-3m$, and their distorted structures possess either a rhombohedral or a trigonal symmetry. The properties of the perovskite systems, the magnetic properties for instance, are usually related to the structural characteristics of the perovskites, such as the octahedra distortions and other displacements of the ions forming the double perovskite structure [15] [16].

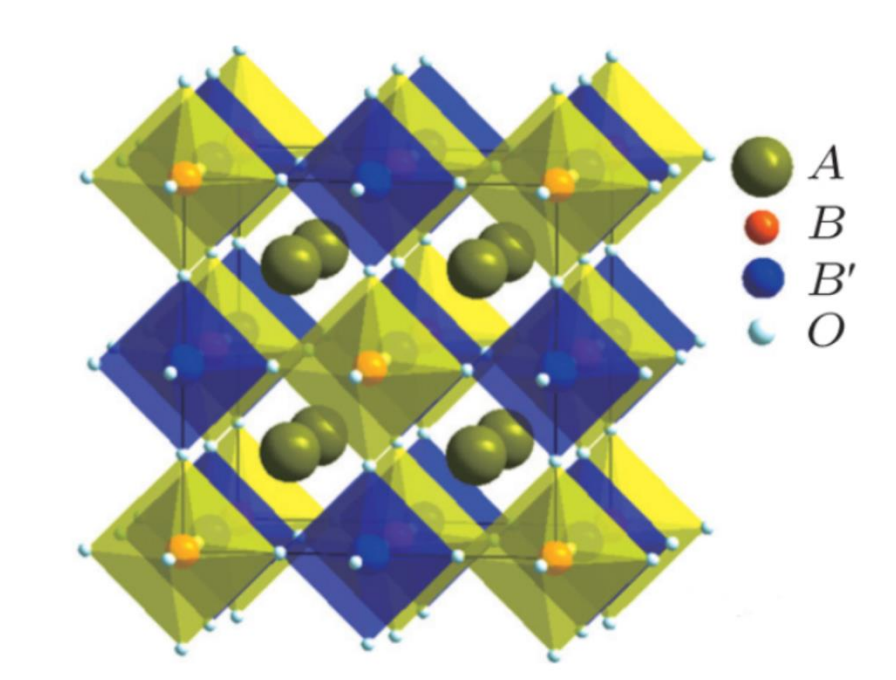


Figure 2.2 Ideal cubic structure of a double perovskite type $A_2BB'O_6$ [17].

2.2 Deviation from the ideal cubic structure and octahedra rotations

Under particular conditions of temperature and pressure, deviations from the ideal cubic perovskite can be computed through the so-called “tolerance factor” by utilizing the experimental values of the ionic radii of **A**, **B** and **X**.

Consider Figure 2.3 and the following atom positions:

- I. B-site occupies each corner of the unit cell at position (0, 0, 0).
- II. An oxygen atoms close to the B-cations taking the position (1/2, 0, 0).
- III. The cation A is located in the center of the unit cell with atomic coordinate (1/2, 1/2, 1/2).

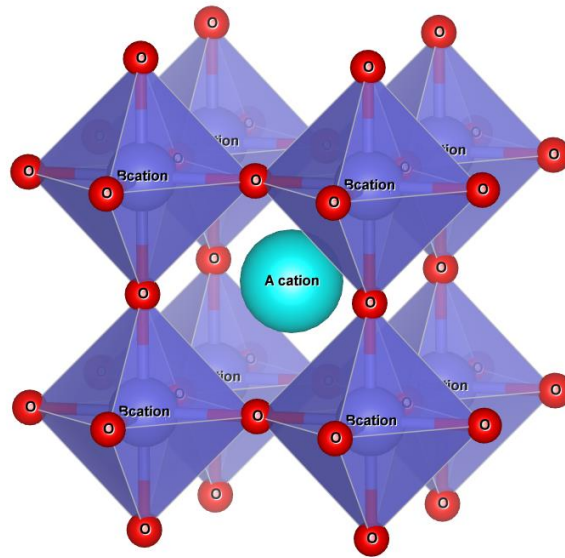


Figure 2.3 schematic representation for an ideal cubic perovskite

One sees that the A-O distance equals $1/\sqrt{2}$ while B-O is equal to $1/2$.

Assuming that the lattice parameter of the unit cell is determined by the ionic radii, for a perfectly closed packed perovskite, the relation between the atomic radii is given by the following equation [18]

$$R_A + R_B = \sqrt{2}(R_B + R_X)$$

where R_A , R_B and R_X are the ionic radius of A, B cations and X anion, respectively.

The tolerance factor, which was introduced by Goldschmidt in order to quantify the deviation from an ideal perovskite structure, is defined as [19]:

$$t = \frac{R_A + R_B}{\sqrt{2}(R_B + R_X)}$$

with $t = 1$ for an ideal cubic perovskite structure.

If $0.9 < t \leq 1$, we have an ideal cubic perovskite phase, for example SrTiO_3 . If $t > 1$ (A too large, or B too small), then the structure becomes tetragonal or hexagonal. For $0.71 < t < 0.9$ (A ions too small to fit into B ion interstices), the structure is either orthorhombic or rhombohedral. Values of t smaller than 0.71 result in crystal structure that are not perovskite anymore (e.g. FeTiO_3 has a trigonal ilmenite structure). Values outside the range for ideal cubic perovskite structure lead to oxygen octahedra rotations. Rotating the oxygen octahedra (BO_6) plays a fundamental role in determining various perovskite properties. To reach a state having a lower energy, perovskite structures have to undergo various types of distortions. The most important are those involving: (i) ionic displacements, in which the transition elements move out from their equilibrium position and (ii) rotations of the octahedra and/or changes in the octahedra bond lengths.

2.2.1 Jahn-Teller effect

In the ground state, if electronic orbitals are degenerated, the system can adopt another geometric configuration with lower overall symmetry by removing degeneracy in order to further minimize the energy and thus stabilizing the structure. This is called Jahn-Teller (JT) effect. Fundamental cause of distortion in perovskite structure can be understood through two factors: (i) the existence of B-site that undergo through first and second order JT effect. (ii) The stereochemical activity of the lone pair that may present in the cation on A -site. To clarify the first, Let us consider an oxygen

octahedron with a metal cation in the center. Therefore d-orbitals will split up into t_{2g} and e_g orbitals.

The first distortion occurs when the degeneracy is lifted through the stabilization (lowering energy) of d-orbitals, allowing an elongation of B-O bond along the z-axis (lowering energy) and compression of other ligands (higher in energy).

More in details, d-orbitals will split up into t_{2g} and e_g orbitals (Figure 2.4). In the case of undistorted symmetric octahedra, we have two orbitals of higher energy (d_{z^2} , $d_{x^2-y^2}$) which are together called e_g . In addition, there are three orbitals of lower energy (d_{xy} , d_{xz} , d_{yz}) collectively known as t_{2g} . In the case of Cu surrounded by 6 oxygen atoms, e_g orbitals are not equally filled as d_{z^2} is fully occupied while $d_{x^2-y^2}$ is partially filled, as shown in the middle of Figure 2.4.

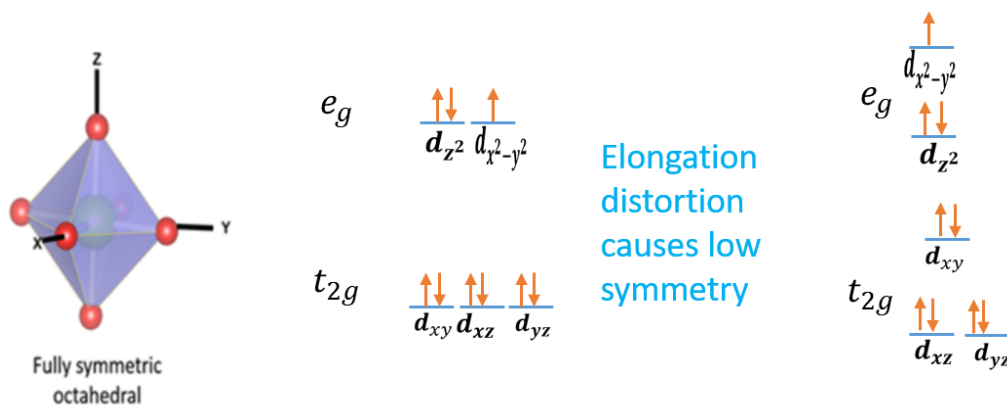


Figure 2.4. Jahn-Teller effect on octahedral Cu^{+2} complex, where the green atom represents Cu^{+2} and red atoms are oxygen.

In that case, the repulsion between the two electrons in d_{z^2} leads to a symmetry distortion, resulting in an axial elongation along the z-direction. Therefore, the bond lengths between the metal and the ligand atoms in the z direction are longer. As a result of the elongation, orbitals in the z direction have lower energy due to the lowering of the energy of orbitals involving a z component, as shown on the right side of Figure 2.4. Second order JT distortions occur when there is a small energy gap between a filled HOMO (highest occupied molecular orbital) and the LUMO (lowest unoccupied molecular orbital). Such distortions can be seen in the change of O-B-O bonds which leads to change in the symmetry group of the perovskite structure [20].

The stereochemical activity of lone pair element (like Bi^{+3} , Sb^{+3}) can cause a structural distortion. In other words, in the presence of 6s lone pair electrons, a crystalline field, affect the arrangement of regular polyhedron that surrounds the cation A. Hence, cation A undergoes a distortion which leads to a variation in the lengths and the angles of O-B-O bonds and a lowering of the energy.

Until now, we have introduced briefly the perovskite structure, as well as their distortions due to the JT effect. Since multiferroics exhibit, by definition, two primary ferroic orders within a single phase, it is important to explain the concept of ferroic materials and their classifications.

2.3 Ferroic Materials

Magnetic material and piezoelectric/pyroelectric/ferroelectric/electric materials, i.e. materials exhibiting a magnetic moment and materials exhibiting an electric polarization have long been considered as different and separate classes of materials. The fact that a material could possess both a ferroelectric and a magnetic ordering simultaneously was first introduced theoretically by Landau and Lifshitz in 1959 [21]. The concept of ferroelastic material (material exhibiting a spontaneous strain, whose configuration can be switched by means of an applied stress), as well as a unified symmetry description of ferroelectric, ferroelastic and ferromagnetic materials, together with the first use of the term 'ferroic' to describe the new class of material including them all, was presented by K. Aizu shortly after [22]. Ferroic materials are classified into ferroelectrics, ferroelastics and ferromagnetics, according to their ordering parameters as well as how they response to an external field. Interestingly, these materials show change in their properties at a critical value of temperature called Curie temperature T_c , and a material symmetry breaking can occur. Ferroic materials are characterized by the existence of domains, each of them having a homogenous crystalline structure and two or more stable states that can be distinguished by the values of some spontaneous macroscopic tensorial physical properties (e.g. polarization or magnetization having different spatial orientation). This spontaneous macroscopic physical property can be switched by means of an appropriate field (e.g. an electric field for ferroelectrics or a magnetic field for ferromagnetics), the

switching between stable states producing some domain dynamics that involves domain walls motion, giving rise to some hysteresis [23].

2.4 Ferroelectric materials

Ferroelectricity was discovered in Rochelle salt by Valasek in 1921 [24]. Generally speaking, ferroelectric materials are dielectrics presenting a spontaneous polarization vector even in the absence of an external electric field. This polarization must have the capability to be reversibly switchable from one state to another, which requires at least two stable states. The reason of ferroelectricity is the presence of a permanent electric dipole moment, the spontaneous polarization being due to the different positive and negative charges barycenters. If the crystal is centrosymmetric (the space group has an inversion center), no polarization occurs because the contributions from the positive charges cancel out for symmetry reasons, and so do the contribution of negative charges. In addition, if the material is subjected to an external electric field, switching of the polarization in the stable state the closest to the direction of the external electric field occurs, and cycling polarization between its 2 stable states (by cycling the electric field) lead to a hysteretic behavior, as illustrated in Figure 2.5 [25]. The physical origin of the hysteretic behavior is the mechanical and electric energy losses that are represented by the imaginary components of the elastic compliance and dielectric permittivity.

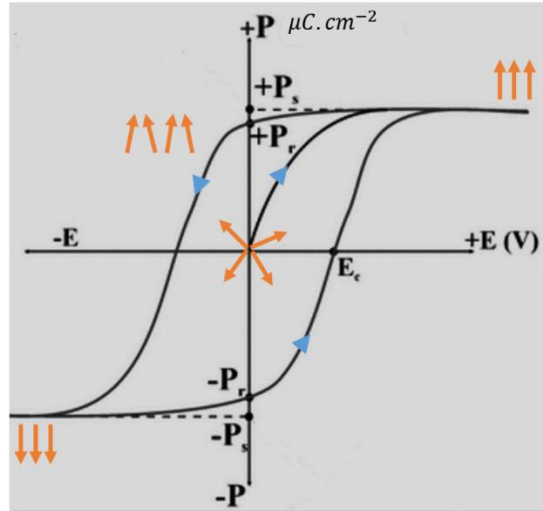


Figure 2.5. Hysteresis loop characteristic of a ferroelectric material, showing the spontaneous polarization P as a function of the applied electric field E .

It is notable that, as the electric field E increases positively, the polarization increases up to a certain limit called saturated polarization P_s . Then, as E decreases to zero, the polarization reaches a particular value called remnant polarization P_r . Conversely, as E further increases negatively, the polarization rises negatively to saturate at $-P_s$. Then, as E goes back to zero, P reaches the remnant polarization $-P_r$. As E further increases positively, P vanishes at a field called coercive electric field E_c .

In the ferroelectric phase of so-called displacive ferroelectrics (in contrast to order-disorder ferroelectrics, not discussed here), the lowest energy structure of a ferroelectric materials below T_c corresponds to a structure where the ions are displaced from their high-symmetry centrosymmetric positions. By definition, at temperature $T = T_c$, the polarization suddenly disappears for a ferroelectric material with a first order transition, and gradually diminishes as T approaches T_c for a ferroelectric material with a second order transition. This results, above T_c , in a paraelectric phase with centrosymmetric symmetry.

The phase transition can be understood when remembering that the stable state is the state with the lowest Gibbs free energy and looking at the Gibbs free energy versus polarization curves for temperatures above T_c , equal to T_c and below T_c , where the two

polarization states $+P_s$ and $-P_s$ take place, as shown in Figure 2.6 for a ferroelectric materials with first order phase transition [26].

Another important characteristics of ferroelectrics is the existence of domains. In ferroelectric materials, there are microscopic domains, and within each of these domains, lined up electric dipoles are uniformly oriented along one of the crystalline directions permitted for the polarization. The application of an external electric field will orient the polarization of all domains in the direction closest to the applied field and polarize the bulk material as a whole. In general, applying a quite high electric field (of the order of hundreds of kV/cm) is necessary in order to reach the polarization saturation, i.e. the situation where all domains have the same orientation of the polarization. When removing the external electric field, most domains tend to keep their polarization oriented in the same direction, producing an effect of memory. The interface region that separates two adjacent domains is called domain wall. the domain wall motion and the energy losses related to this motion also contribute to the hysteretic behavior and to the shape of the hysteresis loop. [27].

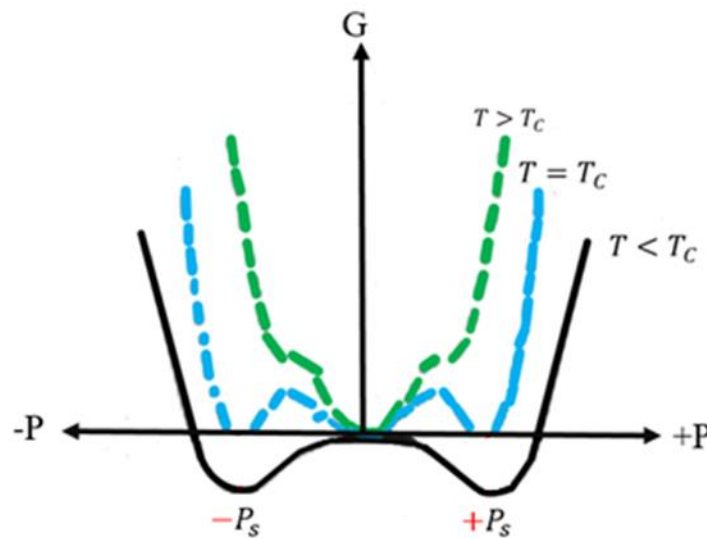


Figure 2.6. Schematic potential well (Gibbs free energy G vs. Polarization P) of a ferroelectric system with first order phase transition for $T > T_c$, $T = T_c$, and $T < T_c$.

2.5 Magnetic Materials

Magnetism is a well-known phenomenon in nature which has attracted the attention of people since immemorial time. Magnetism is a quantum-mechanical phenomenon which occupies a central position in material science. The entities which produce magnetization and magnetize the material are known as spins. Spin is an additional degree of freedom in electronic, atomic and molecular systems. Magnetism mainly results from electrons of the atoms and molecules. Materials can be magnetically categorized into different classes: diamagnetic, paramagnetic, ferromagnetic, antiferromagnetic, and ferrimagnetic, as illustrated in Figure 2.7 [28].

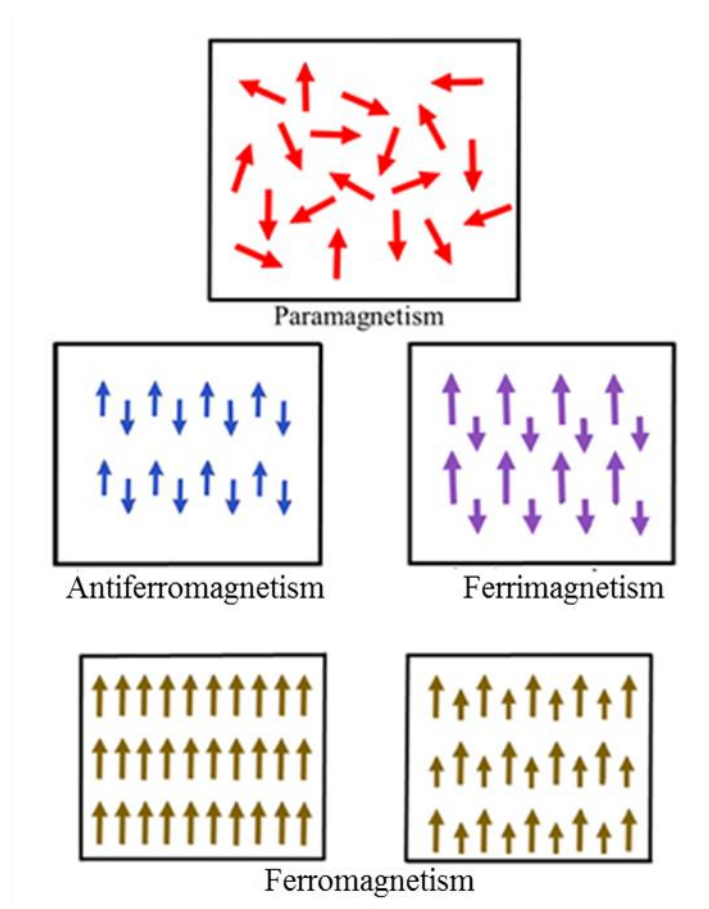


Figure 2.7. Classification of magnetic material according to their magnetic dipole ordering.

In fact, differences in magnetic properties stem from the competition between the effect of thermal agitation and the exchange interaction. Exchange interaction is a quantum-mechanical effect occurring between identical particles. The exchange interaction depends strongly on the spin states S_i and S_j of two interacting electrons according to Heisenberg's Hamiltonian [29] :

$$H = - \sum_{i < j} J_{ij} \mathbf{S}_i \cdot \mathbf{S}_j$$

where J_{ij} is the magnetic exchange integral between S_i and S_j .

When J_{ij} is positive, the interaction is ferromagnetic, while when it is negative the interaction is antiferromagnetic.

2.5.1 Diamagnetic and paramagnetic materials

- I. **Diamagnetic** materials have a zero net magnetic moment in the absence of magnetic field. This property arises in because the electrons in their atomic orbitals are paired with spins in opposite directions. When a diamagnetic material is placed in a uniform magnetic field, it acquires a weak magnetism in the opposite direction to that of the applied magnetic field. While removing the magnetic field, magnetization disappears. It is characterized by its negative magnetic susceptibility of order 10^{-5} which is temperature independent.
- II. **Paramagnetic** materials possess unpaired spins oriented randomly. When the material is subjected to an external magnetic field, the magnetic moments line up in the same direction as the field. They present a small positive susceptibility. As soon as the magnetic field is removed, the individual unpaired spins moments assume again a random orientation and the net material's magnetic moment vanishes. Thermal agitation causes a randomization in the arrangement of the individual magnetic dipole moments so that, when the temperature increases, paramagnetic properties weaken [30].

2.5.2 Ferromagnetic materials

Ferromagnetic materials possess a spontaneous permanent magnetic moment originating from the spins of unpaired electrons in the d and f electron shells of certain atoms. Generally, the dipole magnetic moments in ferromagnetic materials tend to align parallel one to another within domains, due to a strong internal ‘molecular field’, resulting from the quantum-mechanical exchange interaction between neighbouring unpaired electrons. The individual net magnetic moments of each of these domains are randomly oriented to result in a zero global net magnetic moment. When placed in an external magnetic field, the magnetic moments of those domains align along the magnetic field direction. What distinguishes ferromagnetic materials from diamagnetic and paramagnetic materials is that ferromagnetic materials have the ability to remain magnetized and therefore possess a permanent magnetic moment even if the external field is removed. The domain structure optimal energy configuration also depends on the magnetocrystalline anisotropy as Landau and Lifshitz have demonstrated. In the case of magnetic isotropy, the dipole directions will randomly change due to thermal fluctuations and the tendency of the dipoles to align decreases as the temperature rises.

Beyond T_c , ferromagnetic materials undergo a first or second order phase transition and the system becomes paramagnetic, i.e. the system no longer maintains a net spontaneous magnetization unless it is placed in an external magnetic field.

The hysteretic behaviour of the magnetization is due to some resistance to the reorientation of magnetic dipoles (energy loss when the dipoles are forced to rotate away from their easy axis – a direction – determined by the crystallography of the material as well as of its geometrical shape - where they have an energy minimum).

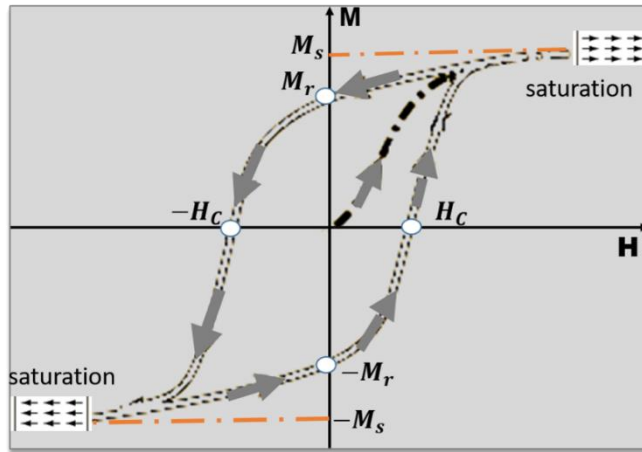


Figure 2.8 Magnetic hysteresis curve of a ferromagnetic material and evolution of the macroscopic magnetization M varies as a function of magnetic field H .

The behavior of the ferromagnetic hysteresis \mathbf{M} vs. \mathbf{H} is similar to that of the \mathbf{P} vs. \mathbf{E} ferroelectric hysteresis shown in Figure 2. 5. As seen in Figure 2.8, there is a remnant value $\pm\mathbf{M}_r$ at $\mathbf{H} = 0$ and a coercive magnetic field $\pm\mathbf{H}_c$ when $\mathbf{M} = 0$.

2.5.3 Ferrimagnetic and antiferromagnetic materials

In antiferromagnetic materials, the magnetic dipoles line up antiparallel, and cancel each other. One of the characteristic features of antiferromagnetic materials is that, at the critical temperature, called Néel temperature T_N , they show an extremely large magnetic susceptibility. Above T_N , antiferromagnetic materials become paramagnetic. In contrast to antiferromagnetic materials, while ferrimagnetic materials have the same antiparallel spins arrangement, the magnitude of the spins oriented in one direction is different from the magnitude of the spins oriented in the opposite direction, so that they don't cancel out and the material displays a net permanent magnetic moment and a hysteresis behaviour similar to that of the ferromagnetic materials below T_c . Most ferrimagnetic materials are ceramic oxides, such as Fe_2O_3 and $\text{Y}_3\text{Fe}_5\text{O}_{12}$. Since transition metals have different numbers of unpaired d-electrons, they are prime candidates to exhibit significant non-zero magnetization [31].

2.6 Multiferroic Materials

The name multiferroic was coined to classify materials in which either two or all three of the ferroic material orders (ferroelectricity, ferromagnetism, and ferroelasticity) are present simultaneously in a single phase [7]. Ignoring the fact that the displacive ferroelectrics, exhibiting both a spontaneous strain and a spontaneous polarization, hence **two** ferroic orders simultaneously, are indeed multiferroic materials according to the definition, the practical definition commonly used today for multiferroics (extended to other long-range orders) is that of a ferroelectric magnetic material or a ferromagnetic or antiferromagnetic ferroelectric materials permitting magnetoelectric effects. Sometimes the term is even used for hetero-phase systems.

Multiferroic materials can be categorized into two classes: type-I and type-II multiferroics. Type I multiferroics, also called “split-order parameter multiferroics”, are materials for which ferroelectricity and magnetism have different origins and set on at different temperatures. They generally have medium to high polarization and have rather weak magnetoelectric coupling (ferroelectricity is due either to lone pairs electrons or in the case of improper ferroelectricity, to charge ordering or to purely structural geometrical distortion). Multiferroics with perovskite and double perovskite structure are *type-I multiferroics* and ferroelectricity is due to lone pairs.

Type-II multiferroics, also called “joint-order parameter multiferroics” are materials for which both ferroelectric and magnetic order are due to the spins (for these materials, magnetic frustration is at the origin of the distortions that lead to a non-centrosymmetric structure and to ferroelectricity). Type-II multiferroics therefore exhibit a robust “built-in” coupling between polarization and magnetic order, but a very small spontaneous polarization [32].

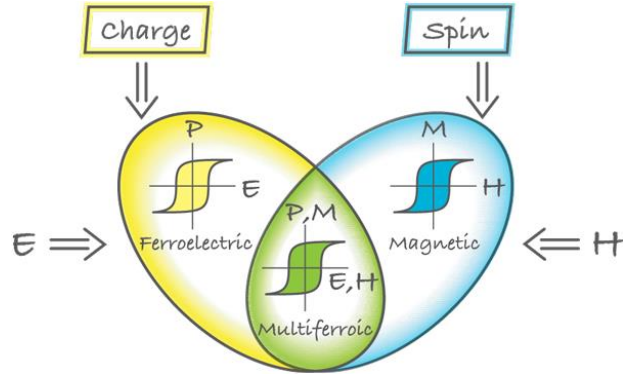


Figure 2.9. Schematics representation of multiferroics (green color) combining the properties of ferroelectrics (blue color) and of magnetic materials (yellow color), i.e. exhibiting both magnetic and ferroelectric hysteresis loops [32].

This coupling will induce a variation in magnetization in presence of an external electric field and a variation of polarization in presence of an external magnetic field. Many interesting applications could benefit from the coupling between magnetic and ferroelectric properties as, for instance, memory, spintronic devices, and switching elements.

The initial requirement for a material to be a multiferroic is that it must exhibit simultaneously ferroelectric and ferromagnetic properties. Hence, the multiferroic properties are determined by the physical properties that appear in ferromagnetic and ferroelectric materials. Therefore, it is relevant to address the limiting factors in restricting the concurrent presence of ferromagnetism and ferroelectricity [33].

- I. **Symmetry considerations.** In order to allow electric polarization, the structural distortions are such that the crystal is not centrosymmetric (lacking an inversion center). More precisely, spontaneous polarization is produced principally from an asymmetry in the atomic positions of the atoms of the perovskite crystal. From a crystallographic and symmetry group point of view, out of the 32 crystallographic point groups, 21 are non-centrosymmetric (which allow piezoelectricity, with the exception of the cubic point group 432), and 10 are polar (allowing pyroelectricity, i.e. a spontaneous polarization to exist, among which

those for which the polarization can be switched by an electric field are called ferroelectric). To describe magnetism, i.e. not only polar vectors but also axial vectors, the time inversion has to be included as an additional symmetry element. Out of the now 122 point groups (after including the time-inversion symmetry element), 31 allow a permanent polarization, and of the 58 magnetic point groups, 31 allow a spontaneous magnetization (i.e. ferromagnetism, the remaining 27 magnetic group being antiferromagnetic) [34]. Belonging to both ferromagnetic and ferroelectric generalized point group (with time inversion) subsets, only 13 (generalized) point groups allow both properties to exist in the same phase. They are: 1, 2, 2', m, m', 3, 3m', 4, 4m'm', mm'2', 2m'm', 6 and 6m'm'. Materials belonging to one of these 13 point groups are therefore multiferroic, and their point group also allows a linear magnetoelectric effect. However, there are 45 other point groups that allow linear magnetoelectric effects, 33 of which are neither magnetic nor ferroelectric [35].

- II. **Electric vs magnetic properties** Perovskite materials display ferroelectricity mainly because of the structural distortion occurring when cation A and B move with respect to the oxygen octahedra. Thus hybridization is expected to take place between fully occupied O 2p states and unfilled d states of the transition element. Magnetism would be optimal when d shells are partially filled, which result in unpaired electrons .

It has been suggested that, assuming that both the ferroelectric and the magnetic properties originate from the transition metal cations inside the oxygen octahedral cage, the multiferroics properties are prohibited in perovskite materials due to different mechanisms causing ferroelectricity and magnetism, which would impose contradictory conditions on the electron occupancies of the d-shells of these cations. While polarization would require completely empty d-orbitals, magnetism, on the other hand, needs partially filled d-orbitals [36]. Nonetheless, the paradoxical mechanisms leading to a single phase multiferroic system are intricate and far from being understood. Indeed, although this field is relatively young, experimental and theoretical researches have proved that coupling two properties in the same phase is

not impossible. For example, Bi-based perovskite, such as the single perovskite BiFeO_3 (BFO) and the double perovskite BiFeCrO_6 (BFCO) display multiferroic properties at room temperature. The apparent paradox has been resolved by suggesting that ferroelectricity is not originating from the transition metal cations, but from the stereochemically active 6s lone pair electrons of the bismuth cations, the transition metal cation being the cause of the magnetism. In BFO, while ferroelectricity is drastically controlled by the hybridization between the O 2p and empty 6s orbitals of Bi, it has been debated whether magnetoelectric coupling could originate from the existence of cycloidal spin order which allows a coupling between magnetization and polarization even if it has been shown that the linear magnetoelectric effect is inhibited in antiferromagnetic structure.

The case of BFCO will be discussed more in detail in Chapter 3.

2.7 Magnetoelectric Effect

The magnetoelectric coupling is the coupling existing between polarization and magnetization in a single phase or composite material. The direct magnetoelectric effect describes the dependence of the Polarization on the applied magnetic field, while the inverse magnetoelectric effect describes the dependence of the magnetization on the applied electric field. In a single phase multiferroic or magnetoelectric material, the magnetoelectric coupling is an intrinsic material properties, while in the case of composite materials, the magnetoelectric coupling is mostly mediated by the elastic coupling between the piezoelectric/electrostrictive phase (which doesn't necessarily need to be ferroelectric and possess a permanent spontaneous polarization) and the piezomagnetic/magnetostrictive phase (which doesn't necessarily need to be ferromagnetic and have a permanent magnetization).

In multiferroics, the magnetoelectric effect is the coupling between the magnetic and electrical order parameters, namely between the spontaneous polarization and the permanent magnetization. In other words, the direct magnetoelectric response consists in an induced change in the electric polarization \mathbf{P} as a result of an applied magnetic field \mathbf{H} and the inverse magnetoelectric response consists in an induced change in the magnetization \mathbf{M} resulting from an applied electric field \mathbf{E} [37].

2.7.1 Direct and Inverse Magnetoelectric Effect

Considering a conventional material where the direct coupling can be described through Landau and Lifshitz's theory, if the material is subjected to external fields \mathbf{E} and \mathbf{H} , the free energies F can be expressed as follows (where summations are performed over repeated indices):

$$F(E, H) = F_0 - P_i^s E_i - M_i^s H_i - \frac{1}{2} \varepsilon_0 \varepsilon_{ij} E_i E_j - \frac{1}{2} \mu_0 \mu_{ij} M_i M_j - \alpha_{ij} E_i H_j - \frac{1}{2} \beta_{ijk} E_i H_j H_k - \frac{1}{2} \gamma_{ijk} H_i E_j E_k + \dots \quad (2.1)$$

Consider \mathbf{E} and \mathbf{H} as independent variables, the free energy can be written in the differential form $dF = \mathbf{P}d\mathbf{E} + \mathbf{M}d\mathbf{H}$, bearing in mind that magnetoelectric coupling can be established either in terms of $P_j(H_j)$ or in terms of $M_j(E_j)$. Differentiating with respect to E_i , one obtains;

$$P_i(E, H) = -\frac{\partial F}{\partial E_i} = P_i^s + \varepsilon_0 \varepsilon_{ij} E_j + \alpha_{ij} H_j - \frac{1}{2} \beta_{ijk} H_j H_k + \frac{1}{2} \gamma_{ijk} H_i E_j - \dots \quad (2.2)$$

With respect to H_i we have

$$M_i(E, H) = -\frac{\partial F}{\partial H_i} = M_i^s + \mu_0 \mu_{ij} M_j + \alpha^*_{ij} E_j - \frac{1}{2} \beta_{ijk}^* H_j E_i + \frac{1}{2} \gamma_{ijk}^* E_k E_j - \dots \quad (2.3)$$

where P^s and M^s , are the spontaneous polarization and magnetization, respectively. ε is the electrical permittivity, μ is the magnetic permeability, and α (α^*) is the direct (inverse) magnetoelectric susceptibility tensor which describes the linear magnetoelectric effect. Due to the first law of thermodynamics, the inverse and direct magnetoelectric effects should be described with the same linear magnetoelectric coefficient. β (β^*) and γ (γ^*) are third rank tensors describing higher-order magnetoelectric effects. The high-order terms are non-linear terms which govern the complicated magnetoelectric coupling at large fields, but can be neglected at weak fields (linear regime). Furthermore, the two expressions of magnetization and polarization (Eqs. (2.2) and (2.3)) do not include the elastic strain effects, which can be significant as well.

2.7.2 Indirect or Elastically-mediated Magnetoelectric Effect

Besides the direct coupling between the order parameters (**P** and **M**) and the driving forces (**H** and **E**) shown above, a second and indirect coupling between the order parameters and the driving forces can be found. Such coupling is induced elastically by the strain effects that characterize ferroelectric materials, namely the piezoelectric effect, and some magnetic materials characterized by the piezomagnetic or magnetostrictive effect. In such a case, the application of an external field, whether it being electric or magnetic, would induce a deformation via the inverse piezoelectric or magnetostrictive effect, which would in turn affect the magnetization or polarization via the direct magnetostrictive or piezoelectric effects.

This indirect or elastically-mediated magnetoelectric coupling is of great practical interest given how rare single phase multiferroic materials are (and even more so at room temperature and above). Composite multiferroic or magnetoelectric materials are therefore promising candidates for applications. Furthermore, they actually usually exhibit larger magnetoelectric coefficients than single phase materials.

2.8 Potential Applications

Materials combining multiple order parameters paved the way for controlling the electric polarization by means of an applied magnetic field and vice versa, taking advantage of the coexistence and coupling of magnetism and ferroelectricity. In ferroelectric materials, the presence of a spontaneous polarization plays a key role in the design of ferroelectric random access memories (FeRAM).

The binary information storage relies on the use of two or more stable and switchable polarization states with different permanent polarization. Despite its high writing endurance, one of noteworthy issue with ordinary FeRAM memories is connected to its destructive reading process (reading of polarization) [38]. There are also magnetic random access memories (MRAM), in which digital information is encoded by different magnetoresistive states that can be switched by a magnetic field. Due to the large magnetic field required to reverse the magnetoresistive state, these memories consume a considerable amount of energy [39]. Interestingly, while FeRAM shows a fast speed in

writing data, MRAM present valuable properties in terms of reading operations. Multiferroic materials might therefore open the door to explore a new memory device with best functionalities. Multiferroic materials can enhance data storage due to the coexistence of several order parameters. Magnetoelectric coupling thus provides interesting perspectives to develop an ultimate memory device that can combine the advantages of MRAMs and FeRAM. This type of memories was named magnetoelectric (multiferroic as a subsystem) random access memories (MERAMs) [40].

Another possible application of these materials is to design tunnel magnetoresistances in which (ferro) magnetic films are used as a tunnel effect barrier. For example, BFO thin films have been utilized as magnetic tunnel barriers that can be controlled electrically. Such materials would contribute to resolve the high power consumption writing issue encountered in MRAM memories [41]. Alternatively, BiMnO₃ (BMO) could also be used as a tunnel barrier because of its ferromagnetism. In case of no or negligible magnetoelectric coupling, the use of multiferroics can be envisioned to engineer memory devices with four states (two magnetic and two ferroelectric state independently addressable) in order to increase the storage density.

In case of a strong magnetoelectric coupling, multiferroic could be implemented to replace the bulky and power-hungry writing head in magnetic storage disks. Indeed, replacing the magnetic coils (inside which an electric current is circulating to generate the magnetic field) by a voltage-controlled much smaller magnetoelectric device would both reduce the bit size, increasing the storage density and significantly reduce the power consumption of the memory device [42].

2.9 References

1. W. C. Röntgen, "Ueber die durch Bewegung eines im homogenen electrischen Felde befindlichen Dielectricums hervorgerufene electrodynamische Kraft". Ann. Phys. 35: 264. doi:10.1002/andp.18882711003 (1888).
2. N. D. Mathur, J. F. Scott, Magnetoelectric phenomena and devices, Phil. Trans, R. Soc, A 372: 20120453 (2014)

3. L. D. Landau and E. M. Lifshitz, "Electrodynamics of Continuous Media", (Pergamon, Oxford), (1960)
4. I. Dzyaloshinskii , Zh. Exp. Teor. Fiz. 37: 881 (1960)
5. D. N. Astrov, Sov. Phys. JETP 11, 708 (1960)
6. M. Fiebig, "Revival of the magnetoelectric effect". Journal of Physics D: Applied Physics. 38: R123. (2005)
7. H. Schmid, Ferroelectrics 162, 317 (1994)
8. N. A. Hill, J. Phys. Chem. B 104, 6694 (2000)
9. B. Wang, H. Neaton, V. Zheng, S. B. Nagarajan, B. Ogale, D. Liu, V. Viehland, D. G. Vaithyanathan, Schlom, U. V. Waghmare, N. A. Spaldin, K. M. Rabe, M. Wuttig, and R. Ramesh, Science, 299(5613):1719 –1722 (2003)
10. Kimura, T. Goto, H. Shintani, K. Ishizaka, T. Arima, Y. Tokura, Nature, 426, 55- 58 (2003)
11. P. Baettig, C. Ederer, and A. N. Spaldin, Phys.Rev B 72, 214105 (2005)
12. R. Nechache, C. Harnagea, A. Pignolet, F. Normandin. T. Veres, L.-P. Carignan, D. Menard, Appl. Phys. Lett. 89, 102902 (2006)
13. M. Goffinet, J. Íñiguez, P. Ghosez, Phys. Rev. B 86, 024415 (2012)
14. R. S. Roth, Classification of perovskite and other AB₃-type compounds, J Res. NBS, 58, 75-88 (1957)
15. M. T. Anderson, K.B. Greenwood, G.A. Taylor, K.R. Poeppelmeier, Prog. Solid St. Chem. 22, 197-233 (1993)
16. F. K. Patterson, C.W. Moeller, and R. Ward, Inorg. Chem., 2 (1), pp 196–198 (1963)
17. L. Youwen, Chinese Physics B, 25(7): 078108 (2016)
18. T. Sato, S. Takagi, S. Deledda, B. C. Hauback, and Shin-ichi Orimo, Sci. Rep. 6, 23592 (2016)
19. V. M. Goldschmidt, Die gesetze der krystallochemie. Naturwissenschaften, 14(21): 477–485 (1926)
20. Mary C. M. O'Brien , Am. J. Phys, 61, 688 (1993)
21. L.D. Landau, E.M. Lifshitz, "Electrodynamics of Continuous Media", (Pergamon, Cambridge) (1960)
22. K. Aizu, J. Phys. Soc. Japan 32 1287 (1972)
23. L. E Cross, Ferroic Materials and Composites: Past, Present and Future. In: Sōmiya S. (eds) Advanced Ceramics III. Springer, Dordrecht (1990)
24. J. Valasek, Phys.Rev. 17, 475 (1921)

25. M. E. Lines, and A. M. Glass, Principles and Applications of Ferroelectrics and Related Materials, Clarendon Press, Oxford (1977)
26. B. A. Strukov and A. P. Levanuk, Ferroelectric Phenomena in Crystals (Nauka, Moscow, 1995; Springer-Verlag, Berlin, (1998)
27. W. J. Merz, Phys. Rev. 95, 690 (1954)
28. B. D. Cullity, C. D. Graham, Introduction to Magnetic Materials, Wiley-IEEE Press (2008)
29. D. Gignoux, M. Schlenker, Magnetism Fundamentals, Springer (2005)
30. J. Crangle, Magnetic Properties of Solids, London, Edward Arnold Inc (1977)
31. A. Aharoni, "Introduction to the Theory of Ferromagnetism", Oxford University Press (2000)
32. A. J. Dekker, Ferromagnetism, Antiferromagnetism, and Ferrimagnetism. In: Solid State Physics. Palgrave, London (1981)
33. D. Khomskii Physics 2, 20 (2009)
34. N. A. Hill, J. Phys. Chem.B 104, 6694-6709 (2000)
35. V. Kopský, Crystallography and Magnetic Phenomena, Symmetry 7, 125-145 (2015)
36. H.Schmid, on a magnetoelectric classification of materials. International Journal of Magnetism. 4(4), 337-361 (1973)
37. R. Ramesh, N. A Spaldin, Nature Mater. 6, 21 (2007)
38. M. Fiebig, J. Phys. D Appl. Phys. 38, R123 (2005)
39. K.M. Rabe, M. Dawber, and J.F. Scott, Rev. Mod. Phys., 77:1083–1130 (2005)
40. J. Akerman, "APPLIED PHYSICS: Toward a Universal Memory". Science. 308 (5721): 508–510 (2005)
41. X.Chen, A. Hochstrat, P. Borisov, and W. Kleemanna, Appl, Phys. Lett. 89, 202508 (2006)
42. Ming Liu and Nian X, Sun Philos Trans A Math Phys Eng Sci. 372(2009): 20120439 (2014)

Chapter 3. COMPUTATIONAL DETAILS AND RESULTS

This chapter first deals with a brief introduction to the DFT software that we utilized in order to investigate the properties of strained and unstrained BFCO. Then we provide crystallographic background about unstrained BFCO along with its related physical properties, such as stable states, magnetism and polarization. Finally, we discuss the effect of the epitaxial strain on BFCO on the (001) surface of a strontium titanate SrTiO₃ substrate, as the BFCO was first synthesized on this substrate. Under the influence of the epitaxial strain, we look for stable BFCO states and discuss several of their features such as their density of states (DOS), ionic charges and electric polarization.

3.1 Vienna Ab Initio Simulation Package (VASP)

All our calculations were performed with the Vienna ab initio simulation package (VASP) [1][2] within the LSDA+U method. The use of LSDA+U is justified by the fact that the LDA functional guarantees reasonably accurate result in short time. VASP is a commercial software performing DFT calculations within the projector augmented wave method (PAW). The electronic fundamental state is determined by the K-S equation while, for geometry optimization, the forces are calculated by the Hellman-Feynman theorem and the quasi-Newton-Raphson algorithms. [3][4].

VASP is based on the pseudopotential approach, which consists in substituting the coulombic interaction potential of the nucleus and the effects of the core electrons by an effective potential interacting only with the valence electrons. Therefore, the K-S equations are solved only for the valence electrons as only these are involved in the chemical bonds.

It is worth noting that in principle the complete wavefunction evolution is defined through the reciprocal space in terms of an infinite number of Brillouin zone k-points (BZK). The software is able to estimate the state occupancy for each k-point. Because we cannot deal with infinite number of plane waves in practice, we determine an energy cutoff value. Performing a DFT calculation with VASP requires four main input files:

- **INCAR:** includes all parameters that define the calculation.
- **POSCAR:** contains the geometry of the system.

- **POTCAR:** contains the pseudopotentials of most elements in the periodic table, as well as information on the atomic structure, such as atomic masses, valence electrons, cutoff energy, etc.
- **KPOINTS:** specifies the k-points in the Brillouin zone.

3.2 Introduction to $\text{Bi}_2\text{FeCrO}_6$ (BFCO) crystal structure

The double perovskite structure (BFCO) was predicted theoretically to be a promising candidate for showing multiferroic properties. The BFCO unit cell was predicted to have a rhombohedral double perovskite structure ($\text{AB}_2\text{B}'\text{O}_6$) belonging to the $R\bar{3}$ space group, with a lattice constant $a_{\text{rh}} = 5.47 \text{ \AA}$ and angle $\alpha_{\text{rh}} = 60.9^\circ$. The unit cell contains 10 atoms, including Fe^{+3} (d^5) and Cr^{+3} (d^3), two Bi^{+3} atoms and six O^{2-} atoms. Both Fe and Cr occupy the center of octahedra formed by six O^{2-} ions [6].

The charges of the Fe and Cr ions have been determined as follows. Their sum must be +6, considering that the charge of the two Bi is +3, the charge of the six O is -2, since the total charge of the unit cell must be zero. The DFT calculations presented below indicate that the ratio of the Fe charge to the Cr charge is always close to 1, indicating that they have the same +3 charge state.

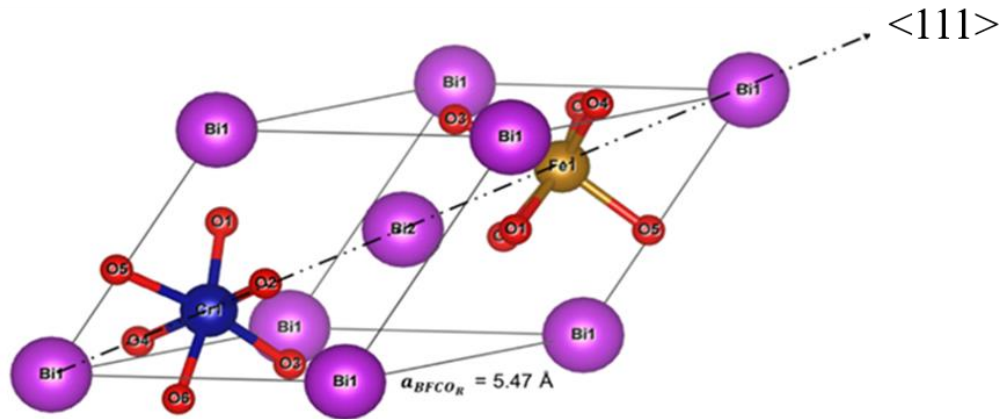


Figure 3.1 BFCO rhombohedral structure and ordering of the transition metals Cr and Fe along the $\langle 111 \rangle$ direction. a_{BFCO_R} , Indicates the lattice constant of the rhombohedron. The 10 atoms of the unit cell are identified ($\text{Bi}_1, \text{Bi}_2, \text{Cr}, \text{Fe}, \text{O}_1, \dots, \text{O}_6$).

The O²⁻ ligands are bonded to the transition metal Fe or Cr, which are d-block elements with unpaired electrons. Crystal field theory (CFT) plays an important role to explain the electric and magnetic properties of perovskite materials which result from distortions of the oxygen octahedra, as well as to describe the degeneracy of d orbitals. The BFCO components and how they contribute to its magnetic and electric properties could be described in the following way:

Essentially, the magnetic properties of BFCO are attributed to the magnetic interaction of the transition metals with their oxygen octahedron. Fe⁺³ (3s² 3p⁶ 3d⁵) and Cr⁺³ (3p⁶ 4s⁰ 3d³) are transition metallic cations having 5 and 3 valence electrons in d-orbitals, respectively. These orbitals are affected by the crystal field of the six O²⁻ ions. This field will split the d orbital in energy with an energy difference Δ between the lower energy orbitals d_{xy} , d_{xz} and d_{yz} , denoted t_{2g} , and the upper energy orbitals d_z^2 and $d_{x^2-y^2}$, which are denoted e_g .

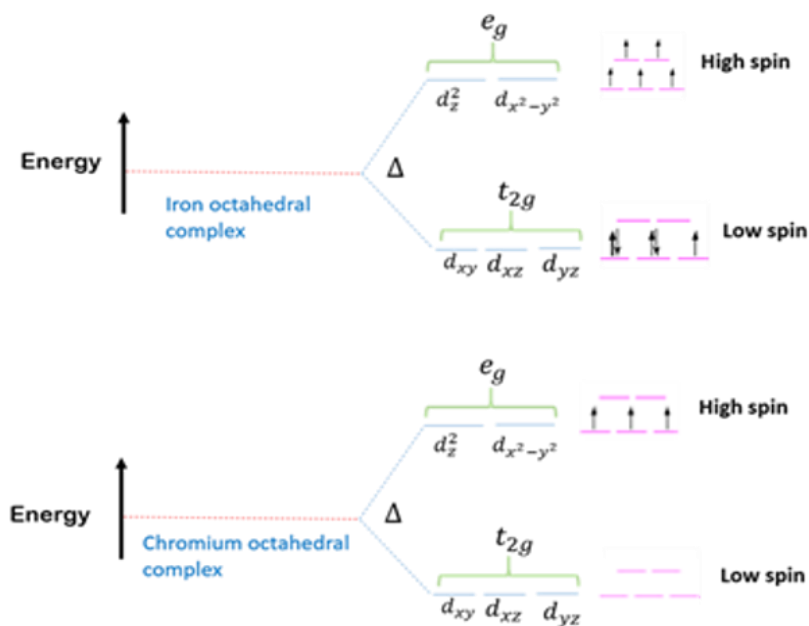


Figure 3.2 Crystal field splitting diagram for Fe⁺³ and Cr⁺³ with spin orientations in the high-spin and low-spin cases^[7].

As shown in Figure 3.2, in the case of Cr^{+3} , the 3 valence d electrons occupy the 3 t_{2g} orbitals, forming a magnetic moment of $3 \mu_B$. In the case of Fe^{+3} , the 5 valence d electrons can occupy two different configurations: high spin and low spin. In the high-spin configuration, the 5 electrons occupy each one of the 5 orbitals t_{2g} and e_g , forming a magnetic moment of $5 \mu_B$, while in the low spin configuration, all the electrons lie in the t_{2g} orbitals, forming pairs with opposite spins in two of them, so that the magnetic moment is only $1 \mu_B$. In the high-spin case, the splitting energy Δ is usually small, thus putting electrons in the e_g orbitals following the Hund's rule is easier than pairing up two electrons into t_{2g} . In contrast, the low spin arrangement occurs when Δ is high and the electronic distribution in this case follows the Aufbau principle. The value of Δ depends on the strength of the repulsive interaction between the outermost electrons in the e_g orbitals and the negatively charged ligand of O^{2-} ions, more than on interactions with electron of the t_{2g} orbital.

The remaining ions Bi^{+3} ($5d^{10}6s^2$) and O^{2-} ($2s^22p^6$) are non-degenerate. Therefore, the effect of the crystal field cannot be observed. Transition metals and oxygen ions interact with each other as it is possible for the O^{2-} p orbitals to overlap with the Cr^{+3} and Fe^{+3} 3d orbitals due to the hybridization in the octahedral environment.

Two magnetic configurations of BFCO can be considered according to the relative spin orientation (up or down) of Fe and Cr. The spin arrangement can produce a ferromagnetic configuration (parallel spins of Fe and Cr) in which, for the ferromagnetic high spin (FMHS) and ferromagnetic low spin (FMLS) cases, the total magnetic moment is $8 \mu_B$ and $4 \mu_B$, respectively. The second configuration is ferrimagnetic (antiparallel spins of Fe and Cr), with the ferrimagnetic low spin (FiMLS) and ferrimagnetic high spin (FiMHS) configurations which have the same total magnetic moment of $2 \mu_B$.

3.3 Calculations of Unstrained BFCO

Full optimization of the BFCO unit cell was performed to determine its electronic, electric and magnetic properties in the unstrained case. As a first step, we optimized the BFCO unit cell without taking the spin into account. This optimized cell was then used as the starting point for the calculation of the four magnetic states described above. For all these calculations, we used the LSDA+U formalism with $8 \times 8 \times 8$ k-points. We used $U = 3 \text{ eV}$

and $J = 0.8$ eV to treat partially occupied orbitals of Fe and Cr as these values (which are typical of insulating materials) have been used in previous works on unconstrained BFCO [8]. Our results prove to be in good agreement with the work of Goffinet et al. [8] despite small differences that can likely be attributed to the differences in the VASP versions used (we used the latest version). The results are summarized in table 3.1.

One observes that the atomic positions of oxygen ions are relatively different from what was reported in Ref. [8]. This means the structural optimization according to the version of the VASP software we used leads to different octahedra distortions due to the free relaxation.

Table 3.1 shows that the ground state belongs to FiMHS while the stability of FMHS is better than that of the two low-spin states. One observes that only 0.162 eV separates the FMHS from the FMHS state. This relatively small separation between the two states

is interesting from the point of view of potential applications since the magnetic moment of the FMHS state is 4 times higher than that of the FMHS state. Therefore, one can wonder whether epitaxial strain could be used to induce a phase transition between FiMHS and FMHS.

Table 3.1 Summary of the electronic properties of the unstrained BFCO system. The system was relaxed by using LSDA+U with $U = 3$ eV and $J = 0.8$ eV. a and α are unit cell parameters whereas Ω denotes the unit cell volume. (x, y, z) indicate the atomic position according to the R_3 space group. μ_{Fe} and μ_{Cr} are the local magnetic moments of Fe and Cr, respectively. The energies are relative to the ground state FiMHS. For comparison, the values between brackets indicate the results which are reported in Ref. **8**.

Phase	FiMHS	FiMLS	FMHS	FMLS
$a(\text{\AA})$	5.466 (5.48)	5.347 (5.37)	5.452 (5.49)	5.348 (5.37)
α in $^\circ$	60.17 (60.04)	60.74 (60.8)	60.38 (60.04)	60.79 (5.37)
$\Omega \text{\AA}^3$	115.96 (166.57)	109.93 (111.33)	115.608 (117.18)	110.12 (111.64)
$x\text{Bi}_1$	0.0 (0.0)	0.0 (0.0)	0.0 (0.0)	0.0 (0.0)
$x\text{Bi}_2$	0.503 (0.503)	0.495 (0.500)	0.501 (0.504)	0.501 (0.49)
$x\text{Fe}$	0.731 (0.732)	0.726 (0.730)	0.731 (0.731)	0.731 (0.731)
$x\text{Cr}$	0.226 (0.226)	0.228 (0.232)	0.226 (0.226)	0.226 (0.232)
$x\text{O}_1$	0.544 (0.544)	0.544 (0.550)	0.544 (0.546)	0.544 (0.550)
$y\text{O}_1$	0.950 (0.950)	0.949 (0.956)	0.951 (0.949)	0.951 (0.953)
$z\text{O}_1$	0.398 (0.398)	0.413 (0.414)	0.398 (0.400)	0.398 (0.413)
$x\text{O}_2$	0.0398 (0.047)	0.0413 (0.046)	0.0398 (0.044)	0.0398 (0.045)
$y\text{O}_2$	0.544 0.905	0.544 0.908	0.544 (0.905)	0.544 (0.908)
$z\text{O}_2$	0.950 (0.447)	0.949 (0.461)	0.951 (0.449)	0.951 (0.457)
$\mu_{\text{Fe}} (\mu\text{B})$	-3.980 (-3.99)	-0.769 (-0.86)	4.15 (4.04)	0.905 (1.02)
$\mu_{\text{Cr}} (\mu\text{B})$	2.542 (+2.55)	2.685 (+2.75)	2.928 (2.86)	2.699 (2.73)
Total (μB)	1.987	1.88	7.66	3.83
Energy, ΔE (meV)	0 (0)	363 (382)	164 (164)	379 (404)

3.3.1 Computing atomic charges

It is well known that atomic charge cannot be measured experimentally because it does not belong to any single physical property. However, through the VASP software, it is possible to calculate the charge of each atom in the system so that the polarization can be calculated, as we will see later. The VASP POTCAR file contains a default radius for each element, called RWIG, which corresponds to the “Wigner–Seitz Radius”. The latter is defined as the radius of a sphere whose volume is equal to the mean volume per atom in a solid. The on-site charges are simply calculated inside the sphere around the atoms. The basis functions inside the sphere are mostly the so-called “projectors” that gives the projector augmented wave (PAW) method. By projecting onto those functions and taking partial sums of just the s, p, and d orbitals, one obtains the partial charges. The charge of each element is calculated by subtracting the charge given in the POTCAR file from the calculation result. The initial charges from the POTCAR files are 15 for Bi, 14 for Fe, 12 for Cr, and 6 for O. The calculated charges are summarized in table 3.2.

Table 3.2.The total charge of each ion in unit of the elementary charge as determined by VASP.

Phase	FIMHS	FIMLS	FMHS	FMLS
Bi_1^{+3}	2.457	2.445	2.459	2.446
Bi_2^{+3}	2.436	2.448	2.44	2.448
Fe^{+3}	1.521	1.32	1.518	1.101
Cr^{+3}	1.19	1.205	1.164	1.211
O_1^{-2}	0.969	0.95	0.969	0.949
O_2^{-2}	1.075	1.08	1.079	1.08
O_3^{-2}	0.964	0.956	0.964	0.956
O_4^{-2}	1.072	1.087	1.076	1.091
O_5^{-2}	0.973	0.979	0.973	0.98
O_6^{-2}	0.939	0.944	0.94	0.943

One observes that the total charge of the unit cell as calculated by VASP is not zero since the charges of the oxygen atoms are positive. This is due to the inaccurate way VASP calculates the charges. Indeed, the calculation of the charges using more sophisticated approaches, such as the Bader method [9], where the charge is calculated inside a more complex volume than the simple Wigner-Seitz sphere, provides more reasonable results. Unfortunately, the Bader method is not implemented in VASP. In the following we will rather use the nominal charges of the ions to calculate the polarization.

3.4 Influence of the Epitaxial Strain on BFCO Single Crystal

Experimentally, the epitaxial strain is used to adjust the lattice constant of the thin film which is expected to fit the lattice constant of the substrate. This type of adjustment induces specific ionic displacements in the thin film at the interface and can modify significantly the properties of the thin film. To simulate the epitaxial strain experiments, SrTiO₃ (STO), whose lattice constant is equal to 3.905 Å, was selected as the substrate. In the original experiments on the synthesis of BFCO, (001)-oriented STO has been chosen because its lattice constant closely matches the lattice constant of BFCO predicted by DFT calculations. Experimentally, Ichikawa et al. made artificial BiFeO₃/BiCrO₃ superlattice grown on STO (111) substrate using the PLD technique. The magnetic measurements at room temperature revealed a magnetization value of 3.7 μ_B/f.u. and a remanent polarization of 60 μC cm⁻² [10]. R. Nechache et al., at INRS, performed magnetic and ferroelectric measurements on single phase BFCO thin film grown on (100)-oriented STO and found a maximum magnetization of 1.9 μ_B/f.u. and a remanent polarization of 55-60 μC cm⁻² [11] in relatively good agreement with the predicted values (2 μ_B/f.u. and ~80 μC cm⁻², respectively).

3.4.1 SrTiO₃ (STO) crystal structure

Strontium titanate STO crystalizes in a single cubic perovskite (ABO₃, space group Pm3m) structure with a lattice parameter $a_{\text{rh}} = 3.905 \text{ \AA}$ and a lattice angle $\alpha_{\text{rh}} = 90^\circ$. As shown in Figure 3.3, this cubic structure is composed of O⁻² ions centered in each face of the cube

formed by the Sr^{+2} ions, occupying the A sites, and Ti^{+4} , occupying the B site octahedrally bonded to the O^{-2} ions [12].

3.4.2 Technical details

As for the unstrained case, the electronic structure calculations were carried out by using the VASP software within parameterization of the projector augmented plane-wave (PAW) method [13]. We considered the local density approximation LSDA+U to describe the partially-filled orbitals of Fe^{+3} ($3s^23p^63d^5$) and Cr^{+3} ($3p^64s^03d^3$). To investigate the electronic and magnetic properties of the strongly correlated system of BFCO, we used a $8 \times 8 \times 8$ Monkhorst-Pack grid of k-points and the energy cutoff was 500 eV. The electronic and ionic convergence conditions were 10^{-8} eV and 10^{-2} eV/Å, respectively. In addition, the values of U and J used here are the same as in the unstrained case discussed above.

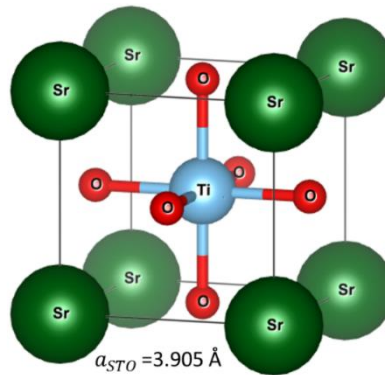


Figure 3.3. Cubic structure of STO with lattice constant = 3.905 Å

3.5 Variation of the energy as a function of the out-of plane-cell size

The BFCO single crystal is epitaxially strained due to the slight lattice mismatch between BFCO and STO. In order to investigate the epitaxial strain in BFCO, we considered the rhombohedral shape inside a fully cubic BFCO structure, as shown in Figure 3.4. This cubic structure sits on the STO substrate, as shown in Figure 3.5. The lattice parameter of STO is experimentally known to be 3.905 Å while that of BFCO in the ground state FiMHS is 5.466 Å (length of the BFCO lattice vectors **a** (red), **b** (green) or **c** (blue) in

Figure 3.4), as indicated in Table 3.1. However, we have to consider the projection of vectors **b** or **c** on the interface plane between the two materials, which is $5.466/\sqrt{2} = 3.865$ Å. Therefore, the STO substrate will slightly stretch BFCO in the interface plane in a proportion of about +1% for the FiMHS state.

The integration of the STO substrate in the DFT calculation proved to be prohibitive in terms of computational time. Indeed, such a calculation needs taking into account a BFCO supercell (i.e. many unit cells) as well as few layers of STO. In order to incorporate the epitaxial strain effect in BFCO *while still doing the calculation for a BFCO unit cell* we proceeded as follows:

The coordinates of the Bi atoms defining the BFCO structure were maintained fixed in the interface plane, which we define as the x - y plane, while their out-of-plane coordinate was varied. With reference to Figure 3.4 this means that the length of the projection of the BFCO lattice vectors **b** (green) and **c** (blue) in the x - y plane (bottom) was set to match the lattice constant of STO, i.e. 3.905 Å, while the length of the lattice vector **a** (red) was $\sqrt{2} \times 3.905 = 5.223$ Å. In addition, the position of the first Bi atom (Bi_1 – see Figure 3.4) was maintained at the position (0, 0, 0). The z -position of Bi_2 (see Figure 3.5) is quantified by the expression

$$z_{\text{Bi}_2} = f \times 3.905 \text{ \AA} \quad (3.1)$$

where the dimensionless factor f was varied manually around 1 in order to find the minimum of energy of the strained BFCO structure. A full DFT calculation was performed for each value of f , so that the positions of all the atoms in the unit cell (except those of the two Bi atoms) were optimized for minimizing the energy of the structure. The value of f corresponding to the absolute minimum of energy thus corresponds to the most stable configuration of BFCO on the STO substrate.

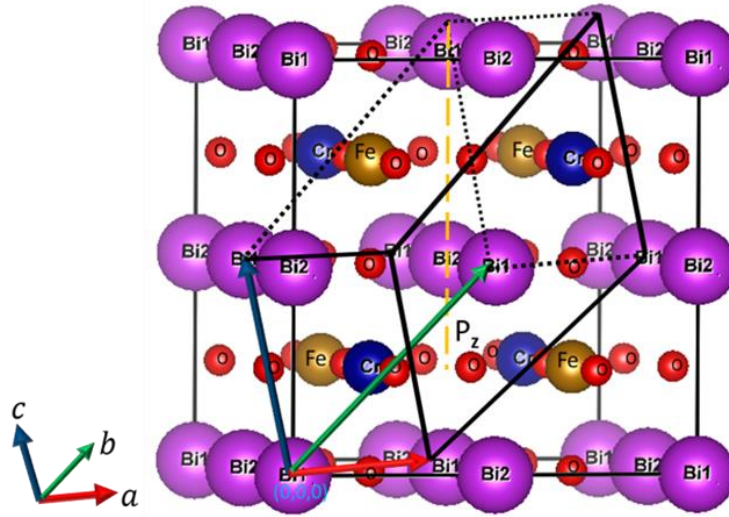


Figure 3.4. Sketch of the rhombohedra in a highly symmetric cubic BFCO.

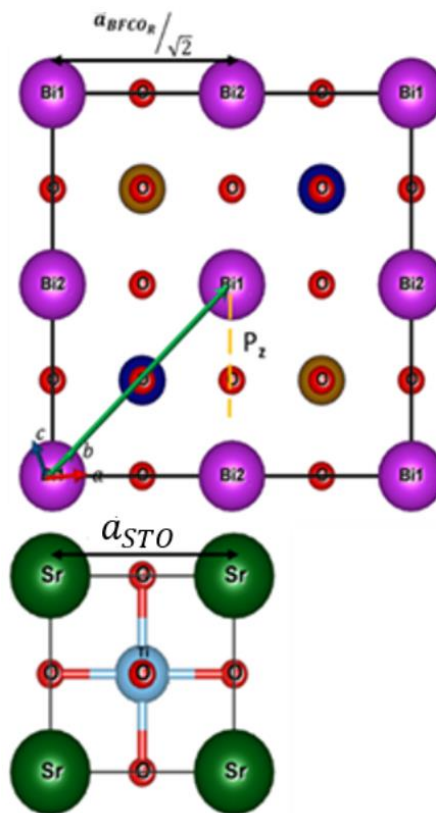


Figure 3.5 BFCO epitaxial film on the STO substrate. Due to epitaxial constraint, $a_{\text{BFCO}}/\sqrt{2} = a_{\text{STO}}$.

We performed calculations for all four phase of BFCO. The energies of the strained BFCO structures as a function of the factor f are shown in Figure 3.6. One observes that the energy follows roughly a parabolic curve as a function of f . Quadratic fits have been performed for each phase and the coefficients of determination R^2 are also indicated in Figure 3.6. The quadratic fits for the four phases are shown together in Figure 3.7.

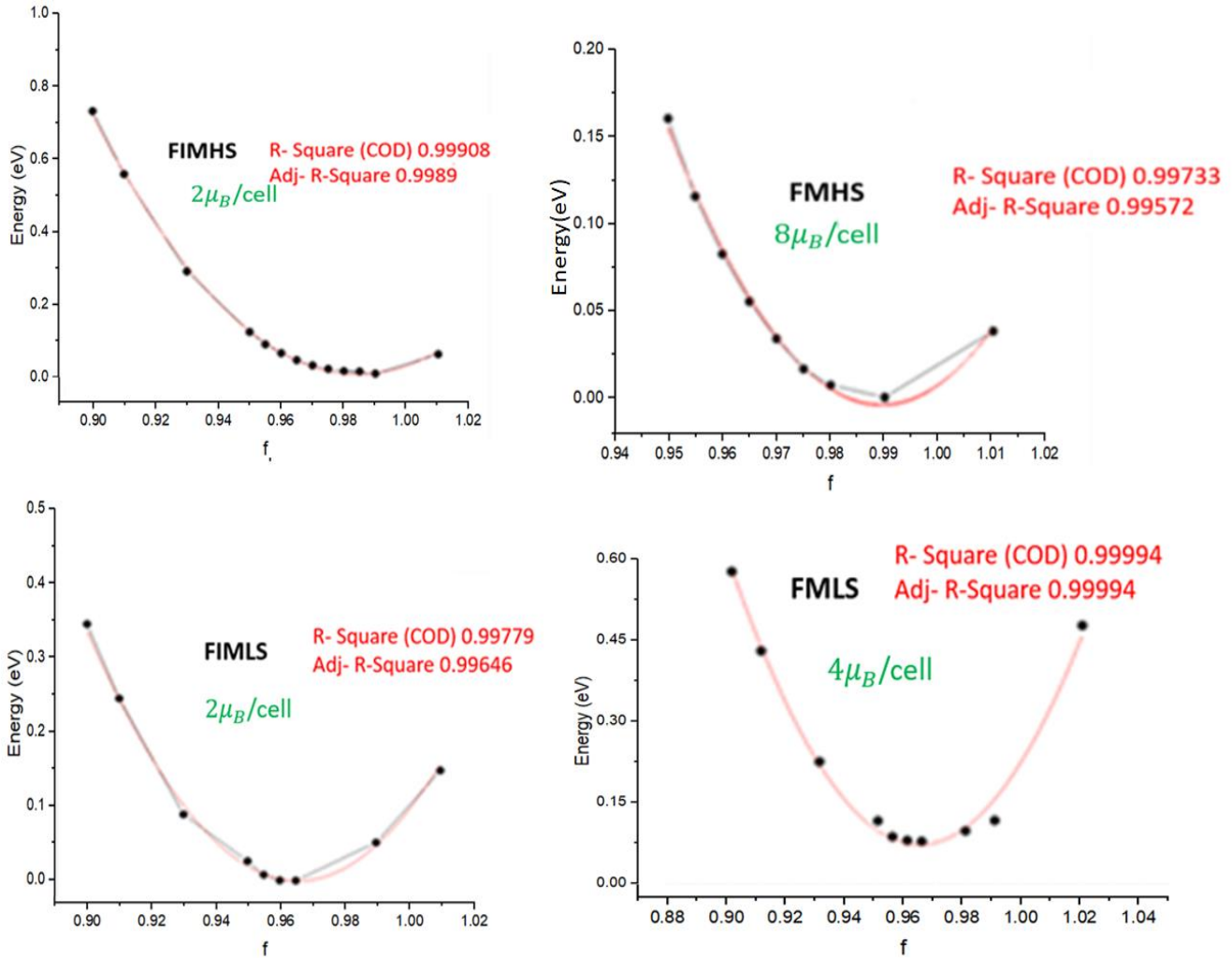


Figure 3.6. The relation between the energy and the factor f . The total magnetic moment per unit cell and the quality of the fits by quartic polynomials are also shown.

The features of the BFCO structures at the energy minima as a function of f (corresponding to the most stable configuration) are listed in Table 3.3. Comparing with Table 3.1, one observes that FimHS remains the ground state of the system. As expected,

we found that the energies of unstrained BFCO are smaller than those of strained BFCO, indicating higher stability of unstrained BFCO. For instance, for the FiMHS state, the energy of unstrained BFCO is $E = -74.932$ eV while for strained BFCO it is $E = -74.924$ eV. The fact that $f < 1$ at the minimum energy means that the out-of-plane size of the unit cell has shrunk in response to the in-plane expansion. However, the volume of the unit cell has increased in all cases. We also observe that the magnetic moment of Fe and Cr, as well as the total magnetic moment remain practically unchanged for all the BFCO phases.

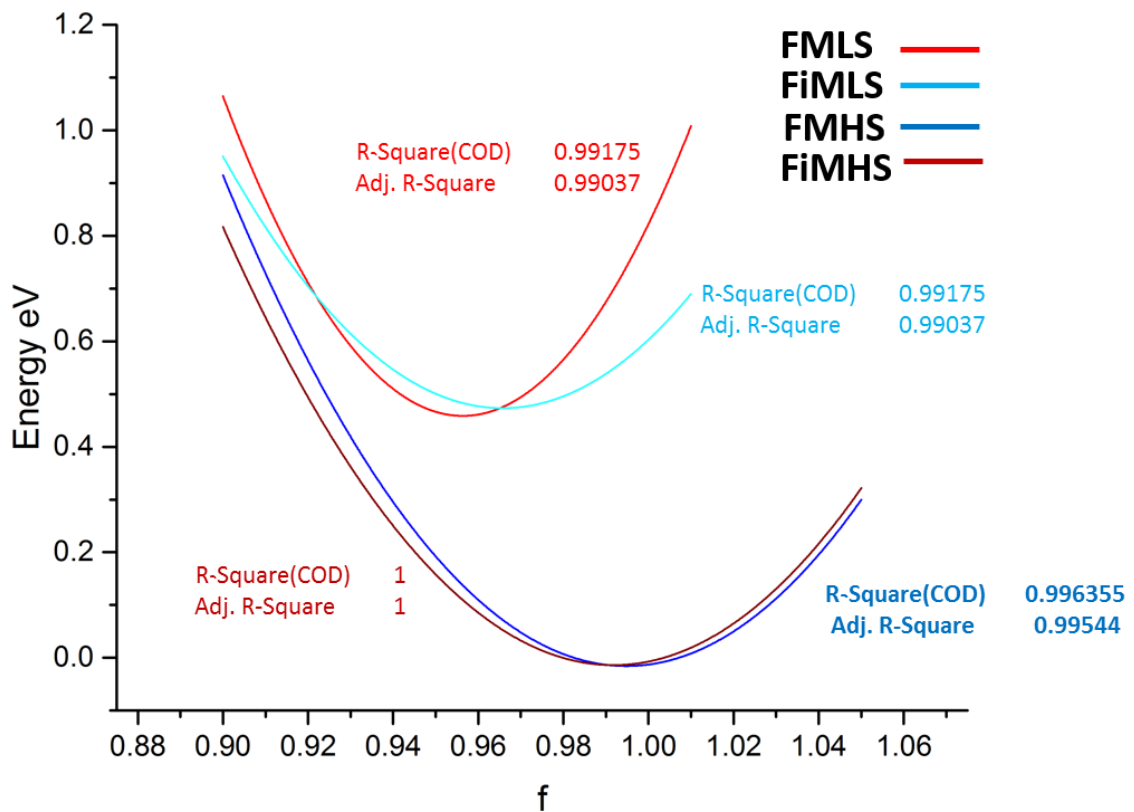


Figure 3.7. Quartic polynomial fits of the calculated energy vs. f for the four phases of BFCO (FiMLS, FMLS, FMHS, and FiMHS) and the quality of the fits.

From Figure 3.7, one observes that the most stable state is FiMHS at low volume ($f < 0.995$) but that FMHS is the most stable at higher volumes. This is very interesting from the point of view of applications, since, as mentioned previously, the FMHS has a nominal magnetic moment of $8 \mu_B$, which is 4 times higher than that of FiMHS.

However, from an experimental point of view, observing this phase transition at large volumes would be a significant challenge. The low-spin phases, FMLS and FiMLS, clearly have higher energies than the high-spin phases within the range of f considered.

Table 3.3. Calculated parameters and properties of strained BFCO. The meaning of the parameters is the same as in table 3.1. a , b , and c are the lattice parameters of the strained quasi-rhombohedral structure.

Phase	FiMHS	FiMLS	FMHS	FMLS
a	5.52	5.525	5.522	5.52
b	5.49	5.42	5.494	5.42
c	5.49	5.42	5.49	5.42
α in $^\circ$	60.42	61.26	60.42	61.26
β in $^\circ$	59.92	59.5	59.92	59.505
γ in $^\circ$	59.92	59.5	59.92	59.5
Ω \AA^3	118.144	115.16	118.144	115.16
$x\text{Bi}_1$	0.000000	0.000000	0.000000	0.000000
$x\text{Bi}_2$	0.493949	0.499184	0.503550	0.497759
$x\text{Fe}$	0.717832	0.726213	0.730373	0.726482
$x\text{Cr}$	0.220180	0.226440	0.224886	0.226153
$x\text{O}_1$	0.519102	0.548141	0.546226	0.547517
$y\text{O}_1$	0.957073	0.947829	0.945244	0.943137
$z\text{O}_1$	0.404169	0.408191	0.400165	0.408680
$x\text{O}_2$	0.400149	0.410464	0.400224	0.408819
$y\text{O}_2$	0.526314	0.541786	0.542132	0.540425
$z\text{O}_2$	0.949443	0.946545	0.947527	0.946496
μFe (μB)	-3.986	-0.864	+4.032	+1.032
μCr (μB)	+2.558	+2.766	+2.868	+2.744
Total (μB)	-1.985	1.905	7.66	3.825
Energy, ΔE (m eV)	0	471	149	476

Table 3.4. Total charge of each ion in unit of the elementary charge as determined by using VASP.

Phase	FIMHS	FIMLS	FMHS	FML
Bi_1^{+3}	2.461	2.462	2.466	2.455
Bi_2^{+3}	2.438	2.464	2.442	2.457
Fe^{+3}	1.542	1.55	1.55	1.279
Cr^{+3}	1.219	1.275	1.252	1.272
O_1^{-2}	1.008	1.001	1.01	1.0
O_2^{-2}	1.016	1.021	1.016	1.021
O_3^{-2}	1.015	1.019	1.015	1.019
O_4^{-2}	1.006	1.023	1.008	1.022
O_5^{-2}	1.007	1.026	1.009	1.024
O_6^{-2}	1.0	1.005	1.004	1.004

We used the same method to calculate the charge of the ions as in the unstrained case. Comparing the calculated charges in the strained case, shown in table 3.4, with those of table 3.2, obtained in the unstrained case, we can observe that most charges have increased, indicating a lower electron localization inside the Wigner-Seitz spheres, which is consistent with the larger cell volume. The opposite occurs in the case O_2 and O_4 , for which the charge has slightly decrease.

3.6 Calculations of the Electric Polarization

As discussed above, the oversimplified approach used by VASP to calculate the ion charges makes that the oxygen ions do not have the expected negative charge and the sum of the charges of the unit cell is therefore not zero. As a consequence, the charges calculated by VASP cannot be used to calculate the polarization, which is directly related to the ion charges. For this reason, we will use the nominal charges of each ion (i.e. +3e for Bi, Fe and Cr and -2e for O) to calculate the polarization.

Now, using the nominal charges, we are able to estimate the electric polarization for each phase. The total polarization \mathbf{P}_T is expressed as the sum of an ion contribution \mathbf{P}_i and electron contribution \mathbf{P}_e :

$$\mathbf{P}_T = \mathbf{P}_i + \mathbf{P}_e \quad (3.2)$$

The ion contribution to polarization is given by:

$$\mathbf{P}_i = \frac{1}{\Omega} \sum_s Z_s^{ion} \mathbf{r}_s \quad (3.3)$$

where Z_s^{ion} = is the charge of the ion s located at the position \mathbf{r}_s in the unit cell, and Ω is the volume of the unit cell. The electron contribution to polarization is formally given by

$$\mathbf{P}_e = \frac{1}{\Omega} \sum_n^{occ} q_n \bar{\mathbf{r}}_n \quad (3.4)$$

In this expression, the sum is over each occupied Wannier function in band n , $\bar{\mathbf{r}}_n$ is the Wannier center, and q_n is the associated electron charge [14].

In principle, \mathbf{P}_e can be calculated within the VASP software by means of the Berry phase method. However, in practice it appears that the calculation can be performed only in certain conditions. One condition is that the band gap of the structure should be “sufficiently” large. Another condition is that the structure has a recognizable symmetry. While these conditions are fulfilled for unstrained BFCO (at least for the FiMHS state), they are not all fulfilled for strained BFCO so that the electron contribution to polarization could not be done by means of the Berry phase method in that case. In particular, the strained BFCO has no longer the pure rhombohedral symmetry of unstrained BFCO (see table 3.3), so that the Berry phase calculation fails within the VASP software. Nevertheless, we can calculate the ion contribution to polarization \mathbf{P}_i and then estimate

the total polarization of the strained BFCO by assuming that the ratio $|\mathbf{P}_T|/|\mathbf{P}_i|$ remains the same as in the unstrained case.

It is important to note that the polarization for periodic systems must be defined through a difference between two connected states in order to lift the ambiguity related to the selection of the set of atoms to consider in the calculation [15]. In our case, we use the difference between the ionic contributions in the strained and unstrained cases

$$\Delta\mathbf{P}_i = \mathbf{P}_{i\text{ strained}} - \mathbf{P}_{i\text{ unstrained}} \quad (3.5)$$

where the ionic polarizations are obtained from Eq. (3.3).

The contribution of each ion to ionic polarization in the unstrained case $\mathbf{P}_{i\text{ unstrained}}$ has been obtained from the difference between the unstrained rhombohedral BFCO and an optimized quasi-cubic structure [14]. We used the nominal charges for Z_s^{ion} . The positions of the ions and the volume of the unit cell are summarized in tables 3.1 and 3.3 for the unstrained and strained cases, respectively (more complete ion positions for the 10 atoms of the unit cell are provided in the VASP output file CONTCAR). Table 3.5 shows the components and modulus of $\Delta\mathbf{P}_i$ as obtained from Eq. (3.5). One observes from table 3.5 that oxygen ions have the major contribution to $\Delta\mathbf{P}_i$. This result is consistent with that of Ref. [14], where it was found that the oxygen atoms provide the main contribution to polarization in unstrained BFCO.

Table 3.5. Contribution of each type of ion to ΔP_i as obtained from Eqs. (3.3) and (3.5).

Phase ΔP_i $\mu\text{C}/\text{cm}^2$	FIMHS	FMHS	FMLS	FIMLS
Bi^{+3}	$ -2.4, -0.96, -0.96 $ = 2.75	$ -1.21, -0.96, -0.96 $ = 1.63	$ -2.7, -0.096, -2.24 $ = 3.5	$ -3.04, -0.24, -0.24 $ = 3.05
Fe^{+3}	$ -4.3, -1.4, -6.4 $ = 7.8	$ -142, 2.0, 1.6 $ = 2.85	$ -6.24, -2.06, -2.03 $ = 6.87	$ -7.3, -2.3, -1.55 $ = 7.8
Cr^{+3}	$ -1.7, -0.8, -0.62 $ = 1.97	$ -0.304, -0.35, -0.432 $ = 0.635	$ -2.7, 0.89, -1.4 $ = 3.16	$ -2.7, -0.92, 1.7 $ = 3.32
O^{-2}	$ 14.7, 6.4, 5.1 $ = 16.8	$ 4.8, 3.3, 16.8 $ = 17.79	$ 22.2, 8.9, 10.09 $ = 25.9	$ 23.7, 10.8, 1.5 $ = 26.08
Total ΔP_i	7.64	18.2	13.8	12.9

Table 3.6 shows the total ionic polarization ΔP_i between strained and unstrained BFCO, as well as the total polarization P_T for the strained and unstrained (in parenthesis) BFCO. The $P_{i_{unstrained}}$ values, the $|\mathbf{P}_T|/|\mathbf{P}_i|$ ratios and the total polarizations in the unstrained case (in parentheses) have been calculated in our group by Dr. Braescu [15]. The total polarization has been obtained through the advanced effective Born charge method (not available in VASP). The calculated polarization values FimHS are in good agreement with published values [7] (the polarizations for the three other BFCO states have been calculated for the first time in Ref. [15]). In order to get an estimate of the total polarization $|\mathbf{P}_T|$ for strained BFCO, we have assumed that the same ratio $|\mathbf{P}_T|/|\mathbf{P}_i|$ applies in the strained and unstrained cases for each BFCO state.

Table 3.6 Polarization results for strained and unstrained BFCO.

<i>phase</i> polarization $\mu\text{C}/\text{cm}^2$	FiMHS	FMHS	FiMLS	FMLS
ΔP_i	7.64	18.2	12.9	13.8
P_i unstrained	54.60	53.46	59.64	61.60
$P_i = P_i$ unstrained + ΔP_i	62.24	71.66	72.54	99.10
Assumed $ \mathbf{P}_T / \mathbf{P}_i $ ratio	1.45	1.46	1.39	1.38
P_T	90.24 (79.24)	104.62 (77.97)	100.83 (83.46)	104.05 (77.97)

Table 3.6 clearly shows a significant increase in the ionic contribution of the polarization, which is reflected in the total polarization. The differences in the polarizations come essentially from the differences in the ion positions inside the two structures since the nominal charges have been used in both cases. Even if the lattice mismatch is on the order of 1%, table 3.6 shows significant changes in the ionic contribution ΔP_i to polarization. Assuming the same ratio $|\mathbf{P}_T|/|\mathbf{P}_i|$ in the strained and unstrained cases, P_T increases by about 13% for the FiMHS state. This large polarization is in agreement with the experimental value of $\sim 90 \mu\text{C}/\text{cm}^2$ obtained from epitaxially grown BFCO thin film on niobium-doped STO (see Figure 10a of Ref. [16]) although it is higher than the polarization of $55\text{--}60 \mu\text{C}/\text{cm}^2$ obtained on undoped STO [10]. One also observes that there is a significant increase in both the ionic and total polarizations of about 35%, 20% and 33% in the cases of FMHS, FiMLS and FMLS, respectively, with respect to the calculated values.

It is possible that the ratio $|\mathbf{P}_T|/|\mathbf{P}_i|$ used for estimating the total polarization P_T is actually overestimated. Nevertheless, if the ratio $|\mathbf{P}_T|/|\mathbf{P}_i|$ is nearly correct, the larger polarization obtained for strained BFCO can be attributed physically to the strong interdependence between the epitaxial strain and polarization, due to distortions induced by strain in the

crystal. For instance, a polarization of $150 \mu\text{C}/\text{cm}^2$ has been measured in strained BFO [17] while the theoretical value for unstrained BFO is $95 \mu\text{C}/\text{cm}^2$ [6], which represents an increase of about 50%.

It is likely that the calculated polarization overestimates the actual film polarization. As stressed in Ref. [17], the polarization measurement depend on the film thickness. Measurements on a thin film provides an average between the polarization of the layers close to the substrate and that from layers father from the substrate. Due to the influence of lattice parameter mismatch, the polarization of layers which are close to the substrate are maximally affected by the epitaxial strain than those far from the substrate. In addition, thin films grown in the laboratory are never as perfect as the computer models.

3.7 Density of state (DOS) calculations for Strained and Unstrained BFCO

We have performed density of state (DOS) calculations within the LSDA+U formalism using the Monkhorst-Pack grid of size $8 \times 8 \times 8$. The main purpose of DOS calculations is to provide further insight into the effect of the epitaxial strain on the electronic properties of BFCO.

DOS calculations for BFCO are shown in Figure 3.10 and Figure 3.11. The DOS for unstrained BFCO (right column) prove to be in overall agreement with the results reported in Ref. [8]. Generally, the splitting of Fe-3d orbitals into the two dissimilar states e_g and t_{2g} is a consequence of the crystal field. As explained above, the high-spin phases are characterized by occupied Cr t_{2g} states and partially unoccupied Fe e_g and t_{2g} , while low-spin phases are characterized by occupied Cr t_{2g} and empty and occupied Fe e_g and t_{2g} . These states are represented in Figure 3.10 and Figure 3.11. It can be seen that epitaxial strain leads to significant changes in DOS. In particular, the distributions of t_{2g} and e_g states around the Fermi level are quite different. In addition, changes are observed in the band gap size for FMHS, from 0.4 eV to 0.3 eV, whereas the FiMHS band gap

remains unchanged. DOS calculations for the low-spin cases show that the Fermi level dips in partially occupied states and the band gap is significantly reduced, so that BFCO tends to have a metallic character. These differences can be ascribed to the large crystal field splitting and strong hybridization between 2p-O and delocalized 3d orbitals.

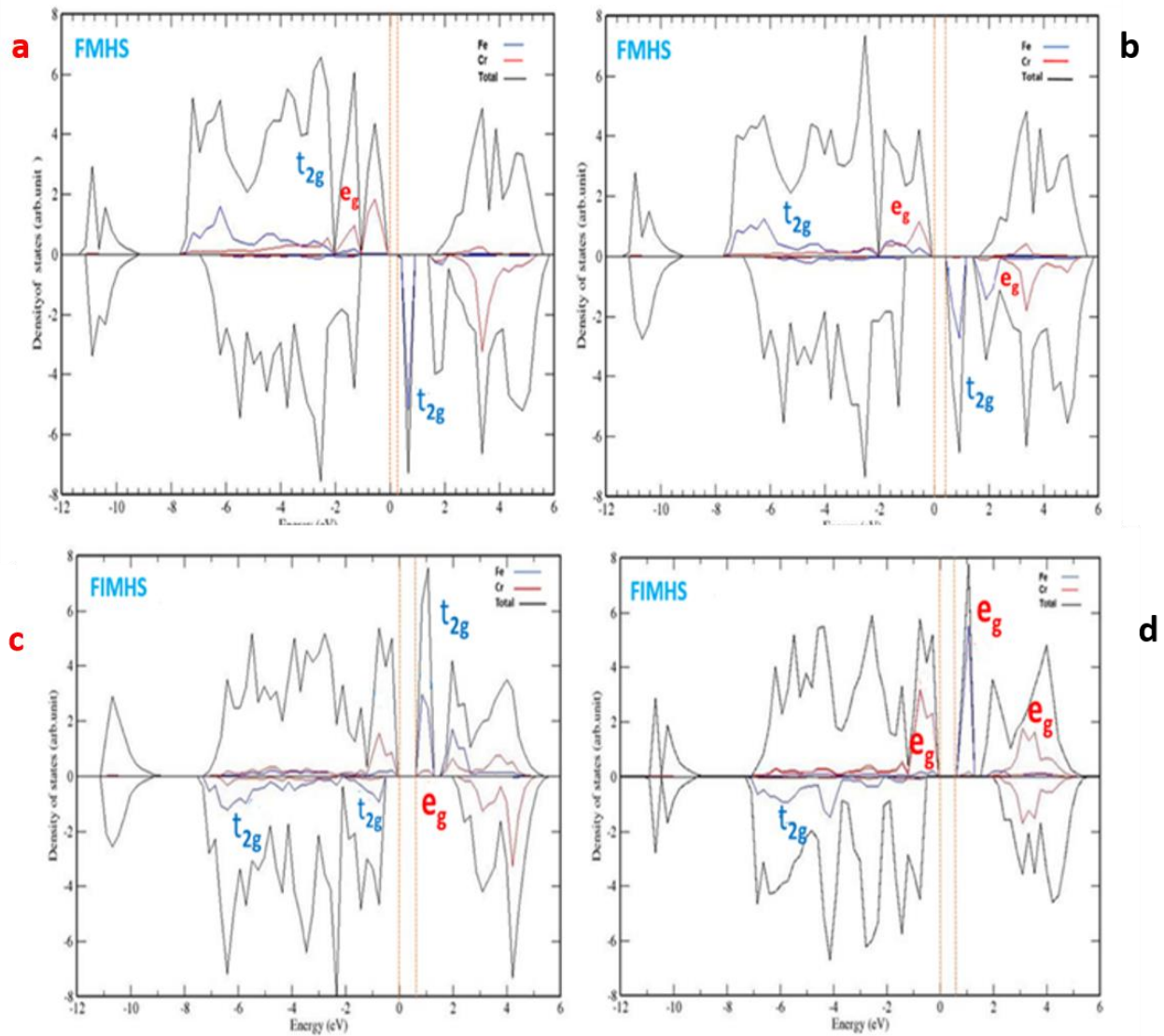


Figure 3.8. Projected DOS of the FIMHS, FMHS, phases of strained BFCO (left) and unstrained BFCO (right). Spins up and down are represented on the positive and negative vertical axis, respectively. Blue, red and black curves pertain to Fe d orbitals, Cr d orbitals, and total DOS, respectively. The DOS calculations are performed with $U = 3$ eV and $J = 0.8$ eV. The blue curve correspond to Fe d orbitals, the red curve to Cr d orbitals and the black curves to the total DOS.

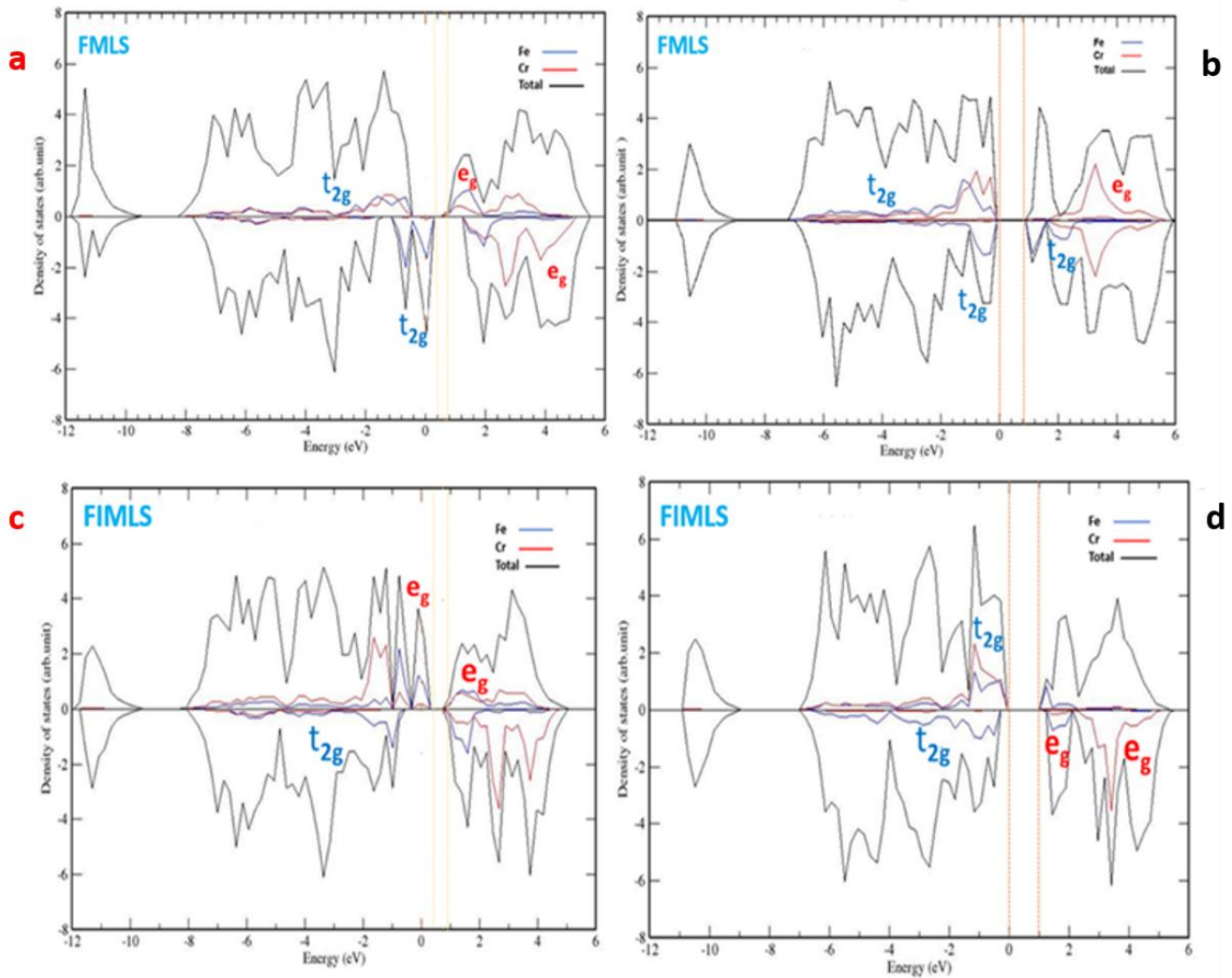


Figure 3.9. Projected DOS of the FIMLS, FMHS, phases of strained BFCO (left) and unstrained BFCO (right). Spins up and down are represented on the positive and negative vertical axis, respectively. Blue, red and black curves pertain to Fe d orbitals, Cr d orbitals, and total DOS, respectively. The DOS calculations are performed with $U = 3$ eV and $J = 0.8$ eV. The blue curve correspond to Fe d orbitals, the red curve to Cr d orbitals and the black curves to the total DOS.

3.8 References

1. G. Kresse and J. Furthmüller, *Comput. Mater. Sci.* **6**, 15 (1996)
2. G. Kresse and D. Joubert, *Phys. Rev. B* **59**, 1758 (1999)
3. R. A. Heaton, J.G. Harrison, and Chun C. Lin, *Phys. Rev. B* **28**, 5992 (1983)s
4. VASP manual , <https://cms.mpi.univie.ac.at/vasp/vasp.pdf>.
5. R. Nechache, C. Nauenheim, U. Lanke, A. Pignolet, F. Rosei, and A. Ruediger, *Journal of Physics: Condensed Matter*, **24**, 142202 (2012)
6. P. Baettig, C. Ederer, and N. A. Spaldin, *Phys. Rev. B* **72**, 214105 (2005)
7. Long G.J, *An Introduction to Crystal Field Effects in Magnetism*, NATO ASI Series (Series C: Mathematical and Physical Sciences), vol 331. Springer, Dordrecht (1991)
8. M. Goffinet, J. Iniguez, and P. Ghosez, *Phys. Rev. B* **86**, 024415 (2012)
9. R. F.W. Bader, *Atoms in Molecules - A quantum theory*, Oxford University Press, New York, (1990)
10. N. Ichikawa, et al , *Japan.Appl.Phys.Express* **1** 101302 (2008)
11. R. Nechache, C. Harnagea, L. P. Carignan, et al, *J. Appl. Phys.* **105**, 061621 (2009)
12. R. D. Leapman, L. A. Grunes, and P. L. Fejes, *Phys. Rev. B* **26**, 614 - 635 (1982)
13. V. I. Anisimov, F. Aryasetiawan, and A. I. Liechtenstein, *J.Phys: Condens. Matter* **9**,767 (1997)
14. N. A. Spaldin, *J. Solid State Chem*, **195**, 2-10, 195 (2012)
15. L. Braescu, PhD thesis , “First-Principles investigation of multiferroic Bi₂FeCrO₆ epitaxial thin films”, INRS-EMT (2018)
16. R. Nechache, C. Harnagea, A. Pignolet, *J. Phys: Condens.Matter*, **24** 096001 (2012)
17. C. Ederer, N. A. Spaldin, *Phy.Rev. Lett*, **95**, 257601 (2005)

Conclusion and Perspectives

In this work we have investigated the properties of unstrained and epitaxially strained $\text{Bi}_2\text{FeCrO}_6$ (BFCO) on a SrTiO_3 (STO) substrate through DFT within the LSDA+U formalism in order to better understand the effects of epitaxial strain on the properties of BFCO. We first investigated unstrained BFCO. Our magnetic calculations showed good agreement with the results that have been reported in literature, the small differences in optimized energies, total magnetic moments, and relaxed ionic positions being probably due to the newer VASP version we used. Although the lattice mismatch between unstrained BFCO and STO is only 1% (STO inducing a slight in-plane stretching of BFCO), our calculations have shown drastic changes on some properties due to the STO strain effect.

In order to calculate the effects of the epitaxial strain of STO on BFCO, we fixed the BFCO rhombohedral cell shape projected on the BFCO-STO interface so as to match the STO lattice parameter, and we varied manually the cell size (i.e. the position of the Bi_2 atom) in the out of plane direction, which was quantified by the scaling parameter f which is proportional to the volume of the cell. A full relaxation of the 10 unit cell atoms (except Bi_1 , which was fixed at (0,0,0), and Bi_2) was performed for each parameter f . A plot of the energy of the BFCO structure as a function of f show approximately parabolic curves for the four BFCO phases, with a clear minimum corresponding to the most stable configuration for each phase. These curves show that FiMHS remains the most stable structure for values of f smaller than that corresponding to the absolute minimum ($f \sim 0.996$), i.e. for smaller cell volumes. The symmetry of the strained BFCO is no longer close to the R_3 rhombohedron. Consequently, we can call this distorted symmetry pseudo-rhombohedral in analogy with the common pseudo-cubic symmetry. DFT calculations showed that epitaxial strain induce a significantly higher ionic, and possibly total, spontaneous polarization. However, the magnetic moment of Fe and Cr as well as the total magnetic moment remains unchanged for all the BFCO phases. In particular, the magnetic moment of FiMHS (most stable state) remains in agreement with the experimental values of $\sim 2 \mu_B/\text{f.u.}$ The DOS shows another aspect of epitaxial strain. We

found that epitaxial strain decreases significantly the band gap in the low-spin cases, while the decrease is smaller in the FMHS case (from 0.4 to 0.3 eV) and negligible in the FiMHS case.

In the future, more detailed simulations could be performed by considering several layers of BFCO instead of a single unit cell, as well as few layers of STO. For instance, the supercell would consist of three layers of BFCO and two layers of STO, as shown in Figure (4.1). This arrangement would possibly allow to understand better the physical interaction between the two materials and the structural variations of BFCO with respect to the distance from the interface.

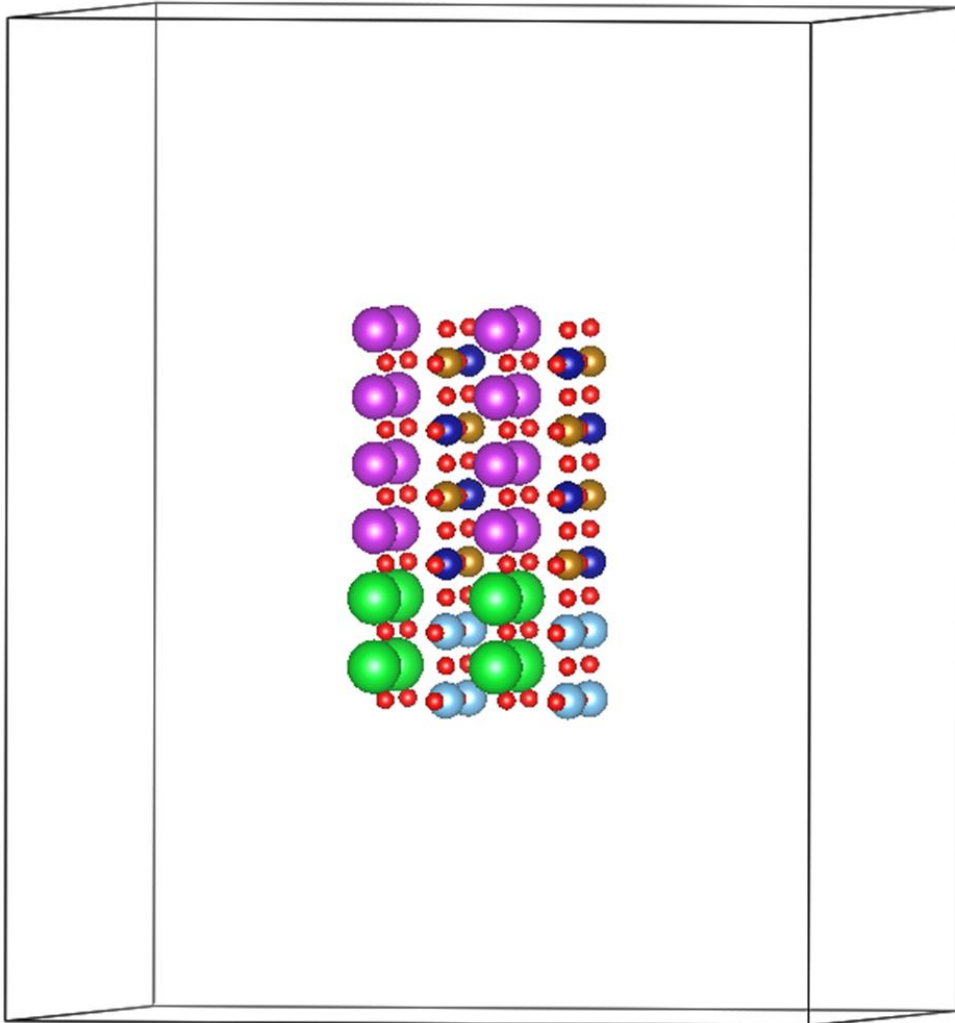


Figure 4.1. BFCO thin film supercell containing three layers of BFCO and two layers STO as a substrate.

Another topic of research would be the tetragonal symmetry of BFCO. Experiments have shown that BFCO can be grown tetragonally (contrary to the rhombohedral symmetry, which, according to DFT studies, is believed to be the most stable state of BFCO). In addition, it would be interesting to investigate other substrates, such as LaAlO_3 (LAO), and $(\text{LaAlO}_3)_{0.3}(\text{Sr}_2\text{AlTaO}_6)_{0.7}$ (LSAT), as well as other orientations of the STO substrate, such as STO(111), to compare with experimental studies.

Résumé du travail de Maîtrise

Le développement continu de théories conduisant à la conception d'algorithmes numériques et de logiciels de structure électronique a permis l'étude de systèmes physiques complexes avec une grande fiabilité et dans un délai raisonnable. La théorie *ab-initio* de la fonctionnelle de la densité ou DFT (pour *Density Functional Theory*), qui repose sur les principes de base de la mécanique quantique, s'est avérée être un outil étonnant, très efficace en science des matériaux ainsi que dans d'autres domaines. Le formalisme DFT repose sur la densité électronique, plutôt que sur la fonction d'onde, afin de déterminer les propriétés de l'état fondamental d'un système d'électrons, sans avoir besoin de paramètres ajustables empiriques.

La DFT a été largement utilisée pour étudier les propriétés d'intérêt dans de nombreux matériaux. En tant que telle, elle a également été parmi les techniques utilisées pour prédire les propriétés d'une famille de matériaux appelés multiferroïques.

La définition formelle d'un matériau multiferroïque est la présence simultanée de plus d'un ordre ferroïque dans la même phase. Dans la plupart des cas, les matériaux multiferroïques montrent un ordre ferroélectrique (souvent accompagné d'un ordre ferroélastique) et un ordre ferromagnétique ou antiferromagnétique [1]. Une telle multiplicité de propriétés physico-chimiques intéressantes présentes dans un seul matériau, avec des applications potentielles prometteuses (telles que le contrôle électrique des propriétés magnétiques du matériau multiferroïque), a attiré un intérêt considérable. Par conséquent, des études théoriques et expérimentales sont actuellement consacrées à acquérir une compréhension fondamentale des propriétés magnétiques et électriques des cristaux multiferroïques monophasiques.

Les propriétés les plus intéressantes des matériaux multiferroïques sont principalement liées à la présence de l'effet magnétoélectrique (couplage entre polarisation électrique et aimantation), ce qui confère à ces matériaux leur grande importance en termes de variété d'applications qu'ils pourraient potentiellement permettre, notamment dans les dispositifs électroniques intégrés. Plusieurs composés à base de bismuth, de la famille $\text{Bi}_2\text{BB}'\text{O}_6$ ayant une structure cristalline de pérovskites doubles, tels que $\text{Bi}_2\text{FeCrO}_6$

(BFCO), $\text{Bi}_2\text{FeMnO}_6$ (BFMO) et $\text{Bi}_2\text{NiMnO}_6$ (BNMO), sont des candidats prometteurs présentant des propriétés multiferroïques [2] [3] [4].

1.0 Introduction

En utilisant la théorie de la fonctionnelle de la densité, nous avons réalisé une étude comparative entre $\text{Bi}_2\text{FeCrO}_6$ (BFCO) sans contrainte et ce même multiferroïque BFCO déformé par des contraintes d'épitaxie lorsqu'il est déposé sur un substrat de SrTiO_3 (STO). La pérovskite double BFCO a été prédite théoriquement comme étant un candidat prometteur pour montrer des propriétés multiferroïques. La maille élémentaire du BFCO proposé aurait une structure de pérovskite double rhomboédrique ($\text{A}_2\text{BB}'\text{O}_6$) appartenant au groupe spatial R_3 , avec une constante de réseau $a_{\text{rh}} = 5,47 \text{ \AA}$ et un angle $\alpha_{\text{rh}} = 60,9^\circ$. La cellule unitaire contient 10 atomes, comprenant Fe^{+3} (d^5) et Cr^{+3} (d^3), deux atomes Bi^{+3} et six atomes O^{2-} . Fe et Cr occupent tous deux le centre des octaèdres formés par six ions O^{2-} (Figure 1).

Les charges des ions Fe et Cr ont été déterminées comme suit. Leur somme doit être +6, considérant que la charge des deux Bi est +3, la charge des six O est -2 [5], puisque la charge totale de la cellule unitaire doit être nulle. Les calculs DFT présentés ci-dessous indiquent que le rapport de la charge de Fe à la charge de Cr est toujours proche de 1, indiquant qu'ils ont le même état de charge +3.

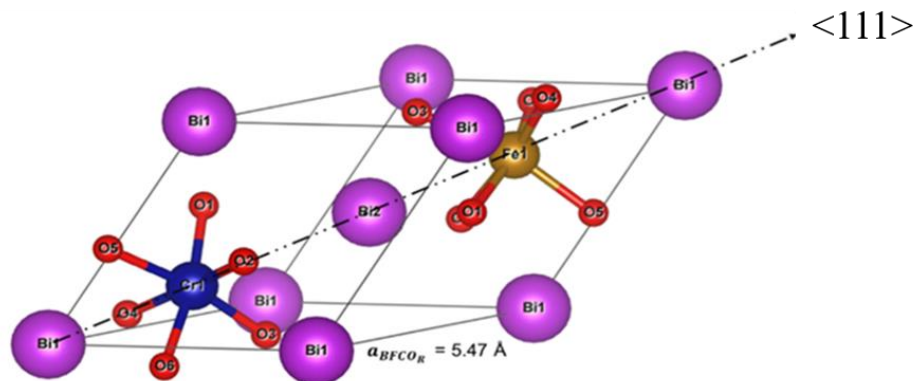


Figure 1. Structure rhomboédrique de BFCO et arrangement ordonné des métaux de transition Cr et Fe le long de la direction $\langle 111 \rangle$. a_{BFCO_R} indique le paramètre de maille du rhomboèdre. Les 10 atomes de la maille élémentaire sont indentifiés ($\text{Bi}_1, \text{Bi}_2, \text{Cr}, \text{Fe}, \text{O}_1, \dots, \text{O}_6$).

2.0 Calculs de BFCO non contraint

Tableau 2. Résumé des propriétés structurales et électroniques du système BFCO non-contraint.

Tous nos calculs ont été effectués avec le logiciel de simulation VASP (pour Vienna ab initio simulation package) dans le formalisme LSDA + U. L'utilisation de LSDA + U est justifiée par le fait que le fonctionnel LDA garantit un résultat raisonnablement précis en peu de temps. VASP est un logiciel commercial effectuant des calculs DFT dans le cadre de la méthode des ondes augmentées par les projecteurs PAW (pour Projector Augmented Wave). L'état fondamental électronique est déterminé par la résolution de l'équation de Kohn-Sham tandis que, pour l'optimisation de la géométrie, les forces sont calculées suivant le théorème de Hellman-Feynman des algorithmes de quasi Newton-Raphson.

L'optimisation complète de la cellule unité de BFCO a été réalisée pour déterminer ses propriétés électroniques, électriques et magnétiques dans le cas sans contrainte. Dans un premier temps, nous avons optimisé la cellule unité de BFCO sans tenir compte du spin. Cette cellule optimisée a ensuite été utilisée comme point de départ pour le calcul des quatre états magnétiques décrits dans le travail, à savoir les états ferrimagnétiques haut spin et bas spin FiMHS et FiMLS ainsi que les états ferromagnétiques haut spin et bas spin FMHS et FMLS. Pour tous ces calculs, nous avons utilisé le formalisme LSDA + U avec grille $8 \times 8 \times 8$ de points k. Nous avons utilisé $U = 3$ eV et $J = 0.8$ eV pour traiter les orbitales partiellement occupées du Fe et du Cr car ces valeurs (typiques des matériaux isolants) ont été utilisées dans des travaux antérieurs sur le BFCO non-contraint [6]. Nos résultats s'avèrent en bon accord avec les travaux de Goffinet et al. [6] malgré de petites différences qui peuvent probablement être attribuées aux différences dans les versions de VASP utilisées (nous avons utilisé la dernière version).

Le Tableau 1 montre que l'état fondamental est FiMHS alors que la stabilité de FMHS est meilleure que celle des deux états bas spin. On observe que seulement 0.162 eV sépare FiMHS de l'état FMHS. Cette séparation relativement faible entre les deux états est intéressante du point de vue des applications potentielles puisque le moment magnétique de l'état FMHS est 4 fois plus élevé que celui de l'état FiMHS. Par conséquent, on peut se demander si les contraintes d'une couche épitaxiée pourraient être utilisées pour induire une transition de phase entre FiMHS et FMHS.

Phase	FiMHS	FiMLS	FMHS	FMLS
a(Å)	5.466 (5.48)	5.347 (5.37)	5.452 (5.49)	5.348 (5.37)
α in °	60.17 (60.04)	60.74 (60.8)	60.38 (60.04)	60.79 (5.37)
Ω Å³	115.96 (166.57)	109.93 (111.33)	115.608 (117.18)	110.12 (111.64)
xBi₁	0.0 (0.0)	0.0 (0.0)	0.0 (0.0)	0.0 (0.0)
xBi₂	0.503 (0.503)	0.495 (0.500)	0.501 (0.504)	0.501 (0.49)
xFe	0.731 (0.732)	0.726 (0.730)	0.731 (0.731)	0.731 (0.731)
xCr	0.226 (0.226)	0.228 (0.232)	0.226 (0.226)	0.226 (0.232)
xO₁	0.544 (0.544)	0.544 (0.550)	0.544 (0.546)	0.544 (0.550)
yO₁	0.950 (0.950)	0.949 (0.956)	0.951 (0.949)	0.951 (0.953)
zO₁	0.398 (0.398)	0.413 (0.414)	0.398 (0.400)	0.398 (0.413)
xO₂	0.0398 (0.047)	0.0413 (0.046)	0.0398 (0.044)	0.0398 (0.045)
yO₂	0.544 0.905	0.544 0.908	0.544 (0.905)	0.544 (0.908)
zO₂	0.950 (0.447)	0.949 (0.461)	0.951 (0.449)	0.951 (0.457)
μFe (μB)	-3.980 (-3.99)	-0.769 (-0.86)	4.15 (4.04)	0.905 (1.02)
μCr (μB)	2.542 (+2.55)	2.685 (+2.75)	2.928 (2.86)	2.699 (2.73)
Total (μB)	1.987	1.88	7.66	3.83
Énergie, ΔE (meV)	0 (0)	363 (382)	164 (164)	379 (404)

3.0 Calcul des charges atomiques

La charge de chaque élément est calculée en soustrayant la charge donnée dans le fichier POTCAR du résultat du calcul. Les charges initiales dans les fichiers POTCAR sont 15 pour Bi, 14 pour Fe, 12 pour Cr et 6 pour O. Les charges calculées sont résumées dans le tableau 2.

On observe que la charge totale de la cellule unitaire telle que calculée par VASP n'est pas nulle puisque les charges des atomes d'oxygène sont positives. Cela est dû à la façon inexacte dont VASP calcule les charges. En effet, le calcul des charges en utilisant des approches plus sophistiquées, comme la méthode de Bader ^[7], où la charge est calculée dans un volume plus complexe que la simple sphère de Wigner-Seitz, fournit des résultats plus raisonnables. Malheureusement, la

méthode Bader n'est pas implémentée dans VASP. Dans ce qui suit, nous utiliserons donc plutôt les charges nominales des ions pour calculer la polarisation.

Tableau 3. Charge totale de chaque ion déterminée par VASP donnée dans l'unité de charge élémentaire.

Phase	FIMHS	FIMLS	FMHS	FMLS
Bi_1^{+3}	2.457	2.445	2.459	2.446
Bi_2^{+3}	2.436	2.448	2.44	2.448
Fe^{+3}	1.521	1.32	1.518	1.101
Cr^{+3}	1.19	1.205	1.164	1.211
O_1^{-2}	0.969	0.95	0.969	0.949
O_2^{-2}	1.075	1.08	1.079	1.08
O_3^{-2}	0.964	0.956	0.964	0.956
O_4^{-2}	1.072	1.087	1.076	1.091
O_5^{-2}	0.973	0.979	0.973	0.98
O_6^{-2}	0.939	0.944	0.94	0.943

4.0 Influence de la contrainte épitaxiale sur BFCO monocristallin

Tout comme dans le cas sans contrainte, les calculs de structure électronique tenant compte de la contrainte épitaxiale ont été réalisés en utilisant le logiciel VASP dans le cadre du paramétrage de la méthode PAW (*Projected Augmented Plane-Wave*). Nous avons considéré l'approximation de densité locale LSDA + U pour décrire les orbitales partiellement remplies de Fe^{+3} ($3s^23p^63d^5$) et de Cr^{+3} ($3p^64s^03d^3$). Pour étudier les propriétés électroniques et magnétiques du système fortement corrélé du BFCO, nous

avons utilisé une grille de points k de Monkhorst-Pack $8 \times 8 \times 8$ et l'énergie de coupure (*cutoff*) était de 500 eV. Les conditions de convergence électronique et ionique étaient respectivement de 10^{-8} eV et 10^{-2} eV / Å. De plus, les valeurs de U et J utilisées ici sont les mêmes que dans le cas sans contrainte discuté ci-dessus.

Le titanate de strontium (STO) cristallise dans une structure de pérovskite cubique simple (ABO_3 , groupe spatial $Pm\bar{3}m$) avec un paramètre de maille $a_{STO} = 3.905$ Å et un angle de réseau $\alpha_{STO} = 90^\circ$. Comme le montre la Figure 2, cette structure cubique est composée d'ions O^{2-} situés au centre de chaque face d'un cube formé par les cations Sr^{+2} , occupant les sites A, et dont le site B situé au centre du cube est occupé par le cation Ti^{+4} , qui est lié de façon octaédrique aux 6 anions O^{2-} [8].

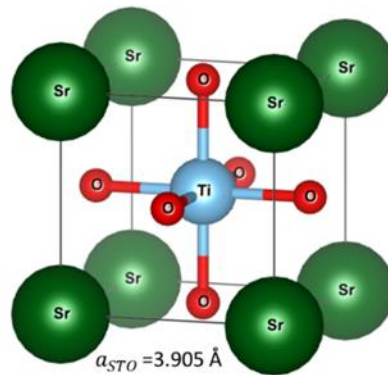


Figure 2. Structure cubique de STO avec constante de réseau $a_{STO} = 3.905$ Å.

Expérimentalement, Ichikawa *et al.* ont déposé des super-réseaux artificiel de couches alternées de $BiFeO_3$ et de $BiCrO_3$ sur substrat STO (111) par ablation laser pulsé (*Pulsed Laser Deposition* – PLD) [9]. Les mesures magnétiques à température ambiante ont révélé une valeur de magnétisation de $3.7 \mu B/f.u.$ et une polarisation résiduelle de $60 \mu C cm^{-2}$. D'autre part, R. Nechache *et al.*, à l'INRS [10], ont effectué des mesures magnétiques et ferroélectriques sur une couche mince de BFCO monphasé, déposée par PLD sur du STO(100), et ils ont trouvé une magnétisation à saturation de $1.9 \mu B/f.u.$ et une polarisation résiduelle de $55-60 \mu C cm^{-2}$, en relativement bon accord avec les valeurs prédites théoriquement ($2 \mu B/f.u$ et $\sim 80 \mu C cm^{-2}$, respectivement).

4.0 Variation de l'énergie en fonction de la taille de la cellule hors-plan

Une couche mince monocristalline de BFCO déposée sur du STO(001) est soumise à une contrainte épitaxiale en raison du léger désaccord de maille (*mismatch*) entre les réseaux cristallins de BFCO et STO. Afin d'étudier la déformation épitaxiale dans le BFCO, et ses conséquences sur les propriétés multiferroïques, nous avons considéré la forme rhomboédrique à l'intérieur d'une structure de BFCO entièrement cubique, comme le montre la Figure 3. Cette structure cubique repose sur le substrat de STO, comme le montre la Figure 4. Le paramètre de réseau du STO est expérimentalement connu pour être 3.905 Å alors que celui du BFCO dans l'état fondamental FiMHS est 5.466 Å (longueur des vecteurs de réseau BFCO a (rouge), b (vert) ou c (bleu) sur la Figure 3), comme indiqué dans le Tableau 1. Cependant, nous devons considérer la projection des vecteurs b et c sur le plan d'interface entre les deux matériaux, soit $5.466 / \sqrt{2} = 3.865$ Å. Par conséquent, le substrat de STO étire légèrement BFCO dans le plan d'interface dans une proportion d'environ + 1% pour l'état FiMHS.

L'intégration du substrat de STO dans le calcul DFT s'est avérée être prohibitive en termes de temps de calcul. En effet, un tel calcul nécessite de prendre en compte une « *supercellule* » de BFCO (c'est-à-dire de nombreuses mailles élémentaires) ainsi que quelques couches de STO. Afin d'incorporer l'effet de déformation épitaxiale dans le BFCO tout en effectuant le calcul pour une maille élémentaire de BFCO, nous avons procédé comme suit :

Les coordonnées des atomes Bi définissant la structure de BFCO ont été maintenues fixes dans le plan d'interface, que nous définissons comme le plan « x-y », tandis que leur coordonnée hors-plan a été modifiée. En référence à la Figure 3, cela signifie que la longueur de la projection des vecteurs de réseau BFCO b (vert) et c (bleu) dans le plan « x-y » (bas) a été réglée pour correspondre à la constante de réseau de STO, soit 3.905 Å, la longueur du vecteur de réseau a (rouge) était $\sqrt{2} \times 3.905 = 5.223$ Å. De plus, la position du premier atome de Bi (Bi_1 – voir Figure 3) a été maintenue à la position (0, 0, 0). La position z de Bi_2 (voir Figure 4) est quantifiée par l'expression :

$$z_{Bi_2} = f \times 3,905 \text{ \AA} \quad (1)$$

où le facteur sans dimension f a été modifié manuellement autour de 1 afin de trouver le minimum d'énergie de la structure de BFCO sous contrainte. Clairement, f est proportionnel au volume de la maille élémentaire, comme le montre la Figure 5. Un calcul DFT complet a été effectué pour chaque valeur de f , de sorte que les positions de tous les atomes dans la maille élémentaire (sauf celles des deux atomes fixes de Bi discutés plus haut) ont été optimisées pour minimiser l'énergie de la structure. La valeur de f correspondant au minimum absolu d'énergie correspond donc à la configuration la plus stable de BFCO épitaxialement contraint par le substrat STO.

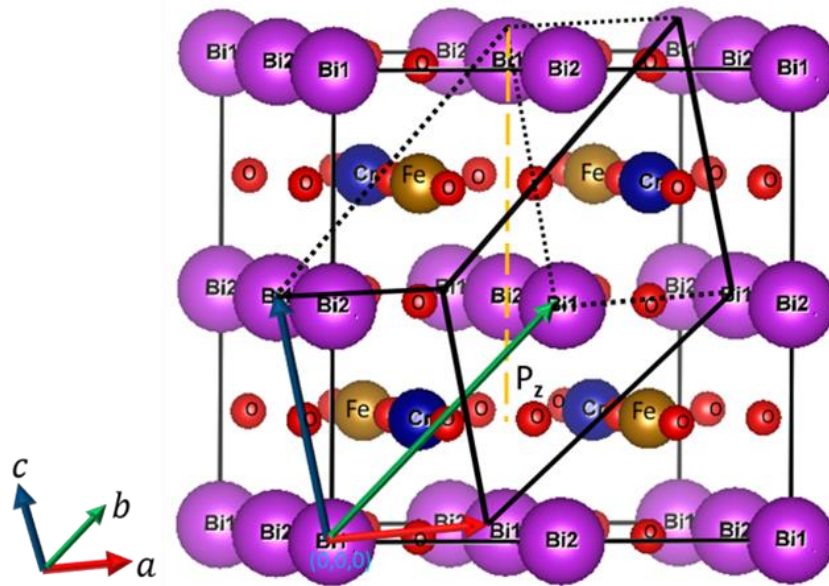


Figure 3. Esquisse des rhomboèdres dans une « supercellule » de BFCO cubique symétrique.

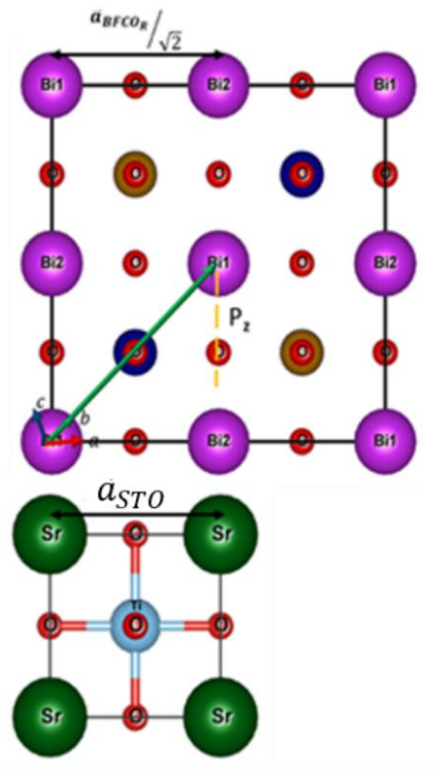


Figure 4. Couche mince de BFCO épitaxié sur un substrat de STO.
 À cause de contraintes d'épitaxie , $a_{BFCO}/\sqrt{2} = a_{STO}$.

Nous avons effectué des calculs pour les quatre états magnétiques de BFCO. Les énergies des structures de BFCO contraintes en fonction du facteur f sont montrées à la Figure 5. On observe que l'énergie suit à peu près une courbe parabolique en fonction de f . Des ajustements par des polynômes quadratiques ont été effectués pour chaque phase et les coefficients de détermination R^2 sont également indiqués dans la Figure 5. Les fonctions polynômiales quadratiques donnant le meilleur ajustement pour les quatre états magnétiques sont montrées ensemble sur la Figure 6.

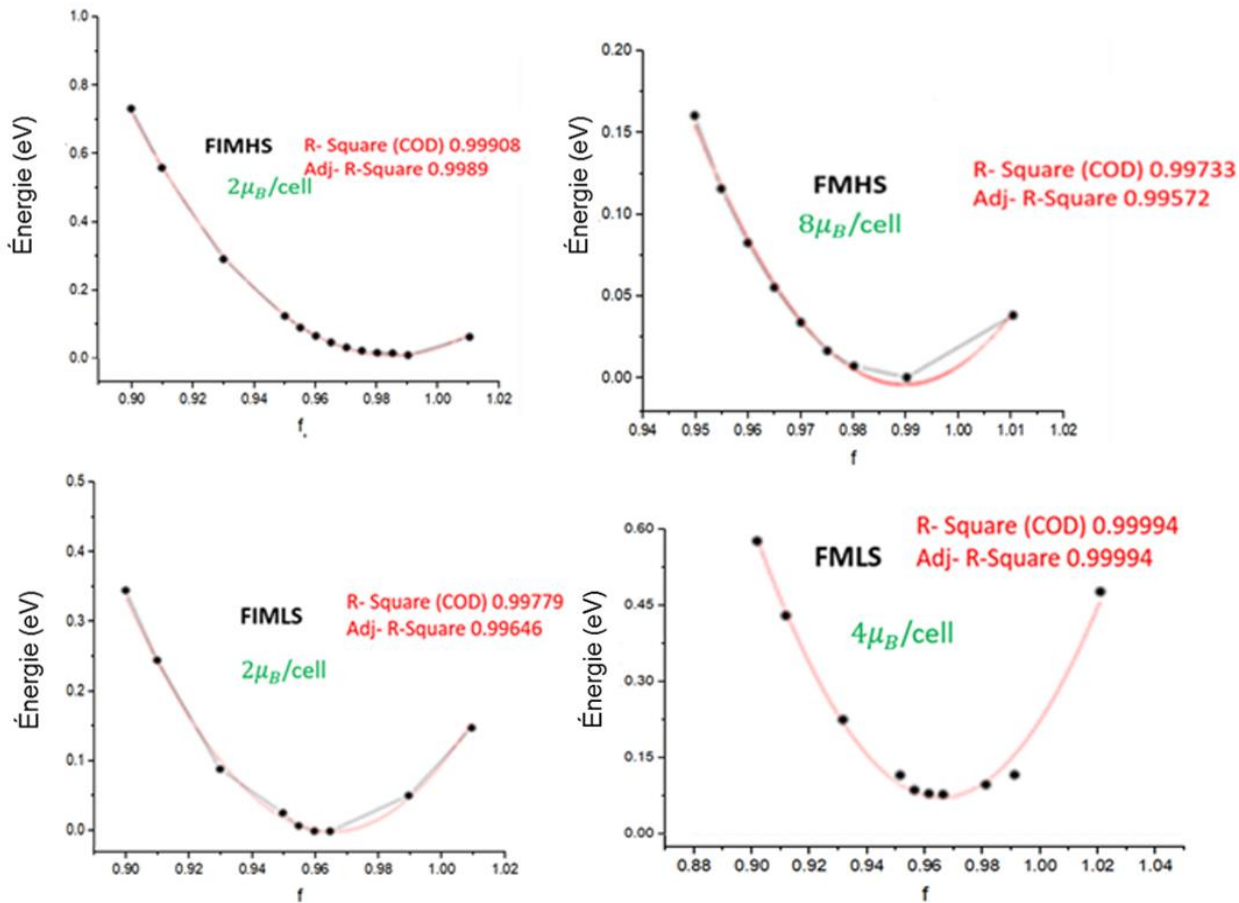


Figure 6. La relation entre l'énergie et le facteur f . Le moment magnétique total par maille élémentaire et la qualité des ajustements par des polynômes quartiques sont également montrés.

Les caractéristiques des structures de BFCO aux minima d'énergie en fonction de f (correspondant à la configuration la plus stable) sont données dans le tableau 3. En comparant avec le tableau 1, on observe que FiMHS reste l'état fondamental du système. Comme prévu, nous avons trouvé que les énergies du BFCO sans contrainte sont plus négatives que celles du BFCO avec contrainte, indiquant une plus grande stabilité du BFCO sans contrainte. Par exemple, pour l'état FiMHS, l'énergie du BFCO sans contrainte est $E = -74.932$ eV alors que pour le BFCO avec contrainte, elle est $E = -74,924$ eV. Le fait que $f < 1$ à l'énergie minimale signifie que la taille hors plan de la maille élémentaire a diminué en réponse à l'expansion dans le plan. Cependant, le volume de la maille élémentaire a augmenté dans tous les cas. Nous observons également que le moment

magnétique de Fe et de Cr, ainsi que le moment magnétique total restent pratiquement inchangés pour toutes les phases BFCO.

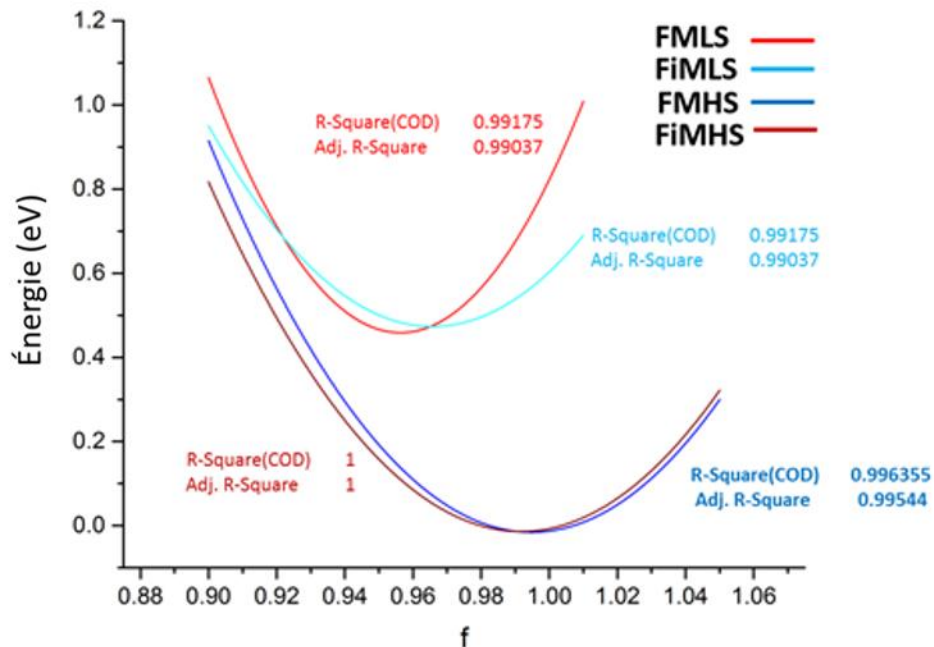


Figure 6. Fonctions polynomiales quadratiques donnant le meilleur ajustement de l'énergie calculée en fonction du paramètre f pour les quatre états magnétiques du BFCO (FiMLS, FMLS, FMHS et FiMHS), ainsi que la qualité des ajustements.

D'après la Figure 7, on observe que l'état le plus stable est FiMHS à faible volume ($f < 0,995$) mais que FMHS est le plus stable à des volumes plus élevés. Ceci est très intéressant du point de vue des applications, puisque, comme mentionné précédemment, le FMHS a un moment magnétique nominal de $8 \mu\text{B}$, ce qui est 4 fois plus élevé que celui du FiMHS. Cependant, d'un point de vue expérimental, provoquer et observer cette transition de phase à grands volumes constitue un défi important.

Les phases bas spin, FMLS et FiMLS, ont clairement des énergies plus élevées que les phases haut spin dans la plage de f considérée.

Tableau 4. Paramètres calculés et propriétés du BFCO avec contraintes. Les valeurs rapportées sont les mêmes que dans le tableau 1 : a, b et c sont les paramètres de maille de la structure quasi-rhomboédrique avec contrainte.

Phase	FiMHS	FiMLS	FMHS	FMLS
<i>a</i>	5.52	5.525	5.522	5.52
<i>b</i>	5.49	5.42	5.494	5.42
<i>c</i>	5.49	5.42	5.49	5.42
α in °	60.42	61.26	60.42	61.26
β in °	59.92	59.5	59.92	59.505
γ in °	59.92	59.5	59.92	59.5
Ω Å³	118.144	115.16	118.144	115.16
<i>x</i>Bi₁	0.000000	0.000000	0.000000	0.000000
<i>x</i>Bi₂	0.493949	0.499184	0.503550	0.497759
<i>x</i>Fe	0.717832	0.726213	0.730373	0.726482
<i>x</i>Cr	0.220180	0.226440	0.224886	0.226153
<i>x</i>O₁	0.519102	0.548141	0.546226	0.547517
<i>y</i>O₁	0.957073	0.947829	0.945244	0.943137
<i>z</i>O₁	0.404169	0.408191	0.400165	0.408680
<i>x</i>O₂	0.400149	0.410464	0.400224	0.408819
<i>y</i>O₂	0.526314	0.541786	0.542132	0.540425
<i>z</i>O₂	0.949443	0.946545	0.947527	0.946496
μFe (μB)	-3.986	-0.864	+4.032	+1.032
μCr (μB)	+2.558	+2.766	+2.868	+2.744
Total (μB)	-1.985	1.905	7.66	3.825
Énergie, ΔE (m eV)	0	471	149	476

Nous avons utilisé la même méthode pour calculer la charge des ions que dans le cas sans contrainte. En comparant les charges calculées dans le cas contraint, montrées dans le tableau 4, avec celles du tableau 2, obtenues dans le cas non contraint, on peut observer que la plupart des charges ont augmenté, indiquant une localisation électronique inférieure dans les sphères de Wigner-Seitz, ce qui est en accord avec le plus grand volume des mailles élémentaires. Le contraire se produit dans le cas O_2 et O_4 , pour lesquels la charge a légèrement diminué.

Tableau 5. Charge totale de chaque ion dans l'unité de la charge élémentaire déterminée par VASP.

4.0 Calculs de la polarisation électrique

Phase	FIMHS	FIMLS	FMHS	FML
Bi_1^{+3}	2.461	2.462	2.466	2.455
Bi_2^{+3}	2.438	2.464	2.442	2.457
Fe^{+3}	1.542	1.55	1.55	1.279
Cr^{+3}	1.219	1.275	1.252	1.272
O_1^{-2}	1.008	1.001	1.01	1.0
O_2^{-2}	1.016	1.021	1.016	1.021
O_3^{-2}	1.015	1.019	1.015	1.019
O_4^{-2}	1.006	1.023	1.008	1.022
O_5^{-2}	1.007	1.026	1.009	1.024
O_6^{-2}	1.0	1.005	1.004	1.004

L'approche trop simplifiée utilisée par VASP pour calculer les charges ioniques fait que les ions d'oxygène n'ont pas la charge négative attendue et que la somme des charges de la maille élémentaire n'est donc pas nulle. Par conséquent, les charges calculées par VASP ne peuvent pas être utilisées pour calculer la polarisation, qui est directement liée aux charges ioniques. Pour cette raison, nous utiliserons les charges nominales de chaque ion (c'est-à-dire + 3e pour Bi, Fe et Cr et -2e pour O) pour calculer la polarisation.

En utilisant les charges nominales, nous sommes en mesure d'estimer la polarisation électrique pour chaque phase. La polarisation totale P_T est exprimée comme la somme d'une contribution ionique P_i et d'une contribution électronique P_e :

$$\mathbf{P}_T = \mathbf{P}_i + \mathbf{P}_e \quad (2)$$

La contribution des ions à la polarisation est donnée par:

$$\mathbf{P}_i = \frac{1}{\Omega} \sum_s Z_s^{ion} \mathbf{r}_s \quad (3)$$

où Z_s^{ion} est la charge des ions situés à la position \mathbf{r}_s dans la maille élémentaire, et Ω est le volume de la maille élémentaire. La contribution des électrons à la polarisation est formellement donnée par [11]

$$\mathbf{P}_e = \frac{1}{\Omega} \sum_n^{occ} q_n \bar{\mathbf{r}}_n \quad (4)$$

Dans cette expression, la somme est sur chaque fonction de Wannier occupée dans la bande n , $\bar{\mathbf{r}}_n$ est le centre de Wannier, et q_n est la charge d'électrons associée. Il est important de noter que la polarisation des systèmes périodiques doit être définie par une différence entre deux états connectés afin de lever l'ambiguïté liée à la sélection de l'ensemble des atomes à prendre en compte dans le calcul [11]. Dans notre cas, nous utilisons la différence entre les contributions ioniques dans les cas contraints et non contraints.

$$\Delta \mathbf{P}_i = \mathbf{P}_{i_{strained}} - \mathbf{P}_{i_{unstrained}} \quad (5)$$

où les polarisations ioniques sont obtenues à partir de l'équation (3).

La contribution de chaque ion à la polarisation ionique dans le cas non contraint $P_{i_{unstrained}}$ a été obtenue à partir de la différence entre le BFCO rhomboédrique sans contrainte et une structure quasi-cubique optimisée [12]. Nous avons utilisé les charges nominales pour Z_s^{ion} . Les positions des ions et le volume de la maille élémentaire sont résumés dans les tableaux 1 et 3 pour les cas non contraints et contraints, respectivement (des positions d'ions plus complètes pour les 10 atomes de la maille élémentaire sont fournies dans le fichier de sortie VASP CONTCAR). Le tableau 5 montre les composants et le module de ΔP_i obtenus à partir de l'équation (5). On observe à partir du tableau 2 que ce sont les ions oxygène qui ont la contribution la plus importante à ΔP_i . Ce résultat est cohérent avec celui de la Réf. [14], où il a été constaté que les atomes d'oxygène fournissent la principale contribution à la polarisation dans le BFCO sans contrainte.

Tableau 5. Apport de chaque type d'ion à ΔP_i tel qu'obtenu à partir des équations (3) et (5).

	FIMHS	FMHS	FMLS	FIMLS
Bi^{+3}	$ -2.4, -0.96, -0.96 $ = 2.75	$ -1.21, -0.96, -0.96 $ = 1.63	$ -2.7, -0.096, -2.24 $ = 3.5	$ -3.04, -0.24, -0.24 $ = 3.05
Fe^{+3}	$ -4.3, -1.4, -6.4 $ = 7.8	$ -142, 2.0, 1.6 $ = 2.85	$ -6.24, -2.06, -2.03 $ = 6.87	$ -7.3, -2.3, -1.55 $ = 7.8
Cr^{+3}	$ -1.7, -0.8, -0.62 $ = 1.97	$ -0.304, -0.35, -0.432 $ = 0.635	$ -2.7, 0.89, -1.4 $ = 3.16	$ -2.7, -0.92, 1.7 $ = 3.32
O^{-2}	$ 14.7, 6.4, 5.1 $ = 16.8	$ 4.8, 3.3, 16.8 $ = 17.79	$ 22.2, 8.9, 10.09 $ = 25.9	$ 23.7, 10.8, 1.5 $ = 26.08
Total ΔP_i	7.64	18.2	13.8	12.9

Le tableau 6 montre la polarisation ionique totale ΔP_i entre le BFCO déformé par les contraintes épitaxiales et le BFCO non contraint, ainsi qu'une estimation de la polarisation totale P_T pour le BFCO contraint et non contraint (entre parenthèses). Les valeurs $P_{i_{unstrained}}$, les ratios $|\mathbf{P}_T| / |\mathbf{P}_i|$ et les polarisations totales dans le cas sans contrainte (entre parenthèses) ont été calculés dans notre groupe par le Dr. Braescu [12]. La polarisation totale a été obtenue grâce à la méthode plus évoluée de la charge efficace de Born (non disponible dans VASP). Les valeurs de polarisation calculées pour FimHS dans le cas sans contrainte sont en bon accord avec les valeurs publiées (les polarisations pour les trois autres états magnétiques du BFCO ont été calculées pour la première fois

dans la Réf. [14]). Afin d'obtenir une estimation de la polarisation totale $|\mathbf{P}_T|$ pour le BFCO contraint, nous avons fait l'hypothèse que le même rapport $|\mathbf{P}_T| / |\mathbf{P}_i|$ s'applique dans les cas sous contrainte et dans le cas sans contrainte pour chaque état magnétique du BFCO.

Tableau 6. Résultats de polarisation pour BFCO déformé et non contraint.

	FiMHS	FMHS	FiMLS	FMLS
ΔP_i	7.64	18.2	12.9	13.8
P_i unstrained	54.60	53.46	59.64	61.60
$P_i = P_i$ unstrained + ΔP_i	62.24	71.66	72.54	99.10
Assumed $ \mathbf{P}_T / \mathbf{P}_i $ ratio	1.45	1.46	1.39	1.38
P_T	90.24 (79.24)	104.62 (77.97)	100.83 (83.46)	104.05 (77.97)

6.0 Densités d'états (DOS) pour le BFCO contraint et non contraint

Nous avons effectué des calculs de la densité d'état (DOS) dans le formalisme LSDA + U en utilisant la grille Monkhorst-Pack de taille $8 \times 8 \times 8$. L'objectif principal des calculs DOS est de fournir un meilleur aperçu de l'effet de la déformation épitaxiale sur les propriétés électroniques du BFCO.

Les calculs DOS pour le BFCO sont illustrés à la Figure 8. Le DOS pour le BFCO sans contrainte (colonne de droite) s'avère globalement en accord avec les résultats rapportés dans la Réf. [6]. Généralement, la levée de la dégénérescence des orbitales Fe-3d et leur séparation dans les deux niveaux d'énergie e_g et t_{2g} est une conséquence du champ cristallin. Comme expliqué ci-dessus, les phases haut spin sont caractérisées par des états Cr t_{2g} occupés et Fe e_g et t_{2g} partiellement inoccupés, tandis que les phases bas spin sont caractérisées par Cr t_{2g} occupé et Fe e_g et t_{2g} respectivement vides et occupés. Les densités

d'états (DOS) « *spin up* » et « *spin down* » pour les quatre phases magnétiques sont représentées dans la Figure 8 pour le cas contraint (gauche) et non contraint (droite).

On peut voir que la contrainte épitaxiale conduit à des changements significatifs dans la DOS. En particulier, les distributions des états t_{2g} et e_g autour du niveau de Fermi sont très différentes. De plus, des changements sont observés dans la largeur de la bande interdite pour FMHS, de 0.4 eV à 0.3 eV, alors que la bande interdite reste inchangée pour FiMHS. Les calculs DOS pour les cas bas spin montrent que le niveau de Fermi plonge dans les états partiellement occupés et que la bande interdite est significativement réduite, de sorte que le BFCO a tendance à avoir un caractère métallique. Ces différences peuvent être attribuées au grand dédoublement du champ cristallin et à l'hybridation forte entre les orbitales 2p de l'oxygène et les orbitales délocalisées 3d de Fe^{3+} et Cr^{3+} .

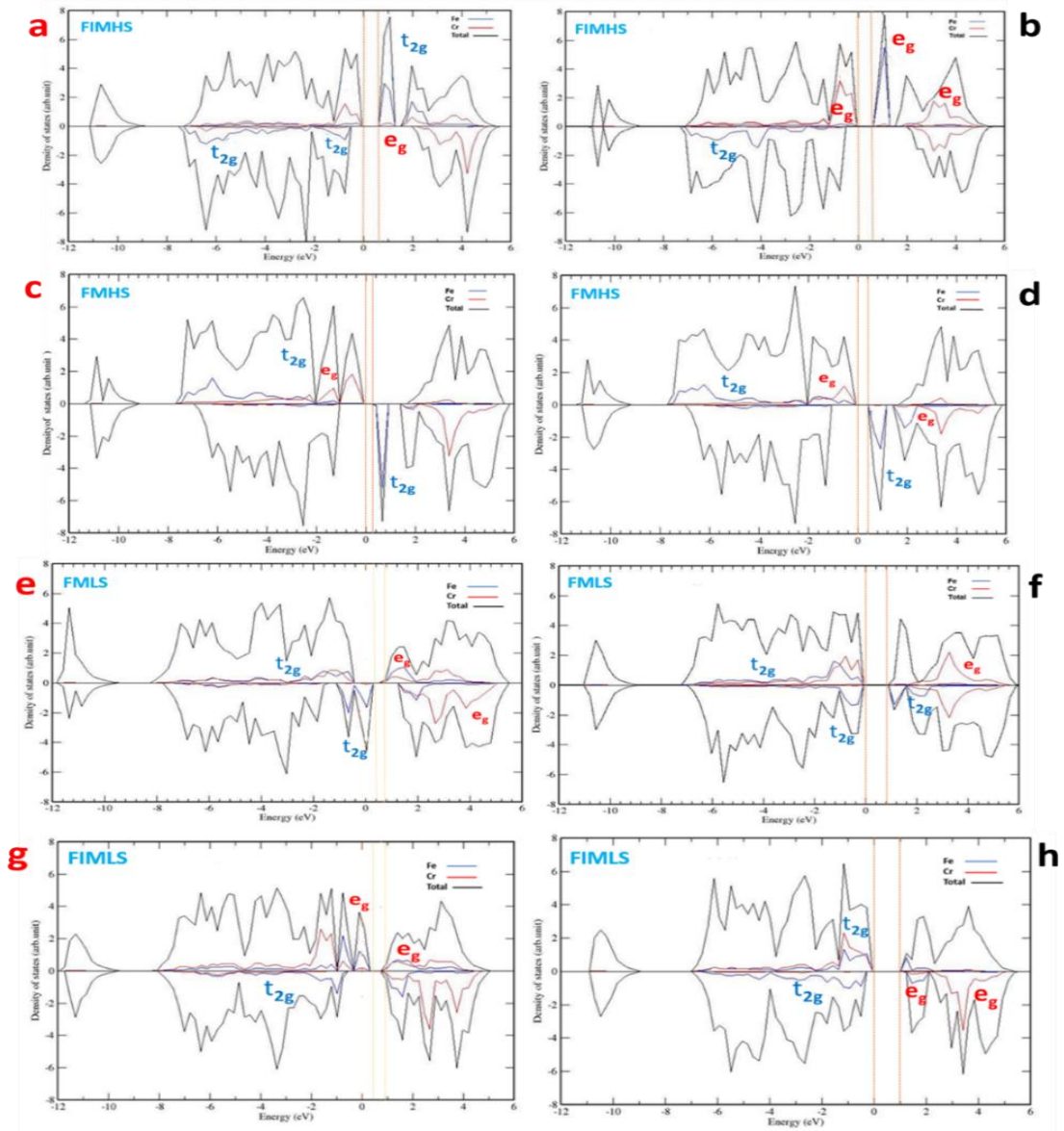


Figure 8. DOS projeté des phases FIMHS, FMHS, FiMLS et FMLS du BFCO avec contrainte (à gauche) et du BFCO sans contrainte (à droite). Les spins up et down sont représentés respectivement sur l'axe vertical positif et négatif. Les courbes bleues, rouges et noires se rapportent respectivement aux orbitales Fe d, aux orbitales Cr d et au DOS total. Les calculs DOS sont effectués avec $U = 3$ eV et $J = 0.8$ eV.

À l'avenir, des simulations plus détaillées pourraient être effectuées en considérant plusieurs couches de BFCO au lieu d'une seule cellule unitaire, ainsi que quelques couches de STO. Une telle configuration permettrait de mieux comprendre l'interaction physique entre les deux matériaux et les variations structurelles du BFCO en fonction de la distance à l'interface.

Un autre sujet de recherche serait d'étudier la phase de symétrie tétragonale du BFCO. Des expériences ont en effet montré que des couches minces de BFCO peuvent posséder une symétrie et une structure tétragonale (à la différence de la symétrie rhomboédrique qui, selon les études DFT, est considérée comme l'état le plus stable du BFCO). En outre, il serait intéressant d'étudier d'autres substrats utilisés expérimentalement, tels que LaAlO_3 (LAO), $(\text{LaAlO}_3)_{0.3}(\text{Sr}_2\text{AlTaO}_6)_{0.7}$ (LSAT), ainsi que d'autres orientations du substrat de STO, telles que STO (111).

References

1. H. Schmid, *Ferroelectrics*, 162,317 (1994)
2. S. Kamba¹, D. Nuzhnyy, R. Nechache, K. Zaveta, D. Niznansky, E. antava, C.Harnagea, and A. Pignolet, *Phys. Rev. B* 77, 104111 (2008)
3. Lei Bi, A. R. Taussig, Hyun-Suk Kim, Lei Wang, G. F. Dionne, D. Bono, K. Persson, G. Ceder, and C. A. Ross, *Phys. Rev. B* 78, 104106 (2008)
4. M. N. Iliev, P. Padhan, and A. Gupta, *Phys. Rev. B* 77, 172303 (2008)
5. P. Baettig, C. Ederer, and N. A. Spaldin, *Phys. Rev. B* 72, 214105 (2005)
6. M. Goffinet, J. Iniguez, and P. Ghosez, *Phys. Rev. B* 86, 024415 (2012)
7. R. F.W. Bader, *Atoms in Molecules - A quantum theory*, Oxford University Press, New York, (1990)
8. R. D. Leapman, L. A. Grunes, and P. L. Fejes, *Phys. Rev. B* 26, 614 - 635 (1982)
9. N. Ichikawa, et al , *Japan.Appl.Phys.Express* 1 101302 (2008)
10. R. Nechache, C. Harnagea, L. P. Carignan, et al, *J. Appl. Phys.* 105, 061621 (2009)
11. N. A. Spaldin, *J. Solid State Chem*, 195, 2-10, 195 (2012)
12. L. Braescu, PhD thesis , “First-Principles investigation of multiferroic $\text{Bi}_2\text{FeCrO}_6$ epitaxial thin films”, INRS-EMT (2018)